



The formation and degradation of active species during methanol conversion over protonated zeotype catalysts

Journal:	<i>Chemical Society Reviews</i>
Manuscript ID:	CS-REV-04-2015-000304.R1
Article Type:	Review Article
Date Submitted by the Author:	11-Jun-2015
Complete List of Authors:	Olsbye, Unni; University of Oslo, Department of Chemistry Svelle, Stian; University of Oslo, Department of Chemistry Lillerud, Karl; University of Oslo, Department of Chemistry Wei, Zhihong; Institute of Coal Chemistry, Chen, Yanyan; Institute of Coal Chemistry, Chinese Academy of Sciences, State Key Laboratory of Coal Conversion Li, Junfen; Institute of Coal Chemistry, Chinese Academy of Sciences, Wang, Jianguo; Institute of Coal Chemistry, Chinese Academy of Sciences, State Key Laboratory of Coal Conversion Fan, Weibin; institute of coal chemistry, XAS,



Journal Name

ARTICLE

The formation and degradation of active species during methanol conversion over protonated zeotype catalysts

Received 00th January 20xx,
Accepted 00th January 20xx

U. Olsbye*,^a S. Svelle,^a K.P. Lillerud,^a Z.H. Wei,² Y.Y. Chen,² J.F. Li,² J.G. Wang,² W.B. Fan**²

DOI: 10.1039/x0xx00000x

www.rsc.org/

The methanol to hydrocarbons (MTH) process provides an efficient route for the conversion of carbon-based feedstocks into olefins, aromatics and gasoline. Still, there is room for improvements in product selectivity and catalytic stability. This task calls for fundamental understanding of the formation, catalytic mechanism and degradation of active sites. The autocatalytic feature of the MTH process implies that hydrocarbons are active species on one hand and deactivating species on the other hand. The steady-state performance of such species has been thoroughly studied and reviewed. However, the mechanism of formation of the initial hydrocarbon species (i.e.; the first C-C bond), and the evolution of active species into deactivating coke species have received less attention. Therefore, this review focuses on the significant progresses recently achieved in these two stages by a combination of theoretical calculations, model studies, operando spectroscopy and catalytic tests.

Introduction

Four decades have passed since the discovery of the methanol to gasoline (MTG) reaction,¹ which inspired the development of the Methanol to Olefins (MTO), Methanol to Propene (MTP), Mobil's olefin-to-gasoline and distillate process (MOGD) and Topsøe's Improved Gasoline synthesis (TIGAS) processes. These processes may commonly be called: the "MTH" (Methanol to Hydrocarbons) process. The MTH process represents a key step in the conversion of any carbonaceous feedstock, via methanol, to a range of hydrocarbons and water, and is currently gaining industrial significance.² Many excellent reviews have been published about the MTH process, covering early studies with focus on industrial development and process chemistry, via two decades of studies focusing on mechanistic insight and shape selectivity, to recent studies devoted to single reaction steps and elucidation of confinement effects by quantum chemistry and molecular dynamics calculations, alone or in combination with experimental studies.²⁻¹⁵

Most recent reviews focus on product formation during steady-state operation of the MTH process, especially on the autocatalytic segment in which products are formed via the so-called "dual-cycle" mechanism (Fig. 1).^{16,17} In the current review, we will focus on two non-steady-state aspects of the MTH reaction, i.e. the formation and degradation of the active state of the catalyst. The review is divided into two parts:

Part 1. The mechanism and catalytic site responsible for the first C-

C bond formation, and the build-up of hydrocarbon pool species. A thorough review of this topic is warranted because it is important for the MTH reaction, and also for the methanol to dimethyl ether (DME) process, where C-C bond formation is detrimental because it triggers the (then undesired) MTH reaction.

Part 2. Catalyst stability towards coke formation. Catalyst deactivation is an integral part of most catalysis studies. However, the autocatalytic nature of the MTH reaction makes quantitative catalyst stability comparisons a challenging task. Therefore, the ambition of Part 2 of this review is to integrate the current knowledge about catalyst deactivation by coke formation on the macro-, meso- and micro-scale.

(Fig. 1)

Part 1:

The mechanism for formation of the first C-C bond

1.1 Recent progress in understanding the hydrocarbon pool mechanism

The key of the MTH process is to control product selectivity and increase the catalytic stability by developing high-performance catalysts and optimizing reaction conditions. This requires a clear understanding of the reaction mechanism, that is, how the active sites are formed and they catalyze the reaction. However, it is a huge challenge because it involves in many elementary reactions occurring in both competing and consecutive ways throughout the whole process.^{4,12,14} The theoretical calculations show that all the proposed direct mechanisms, e.g. carbene, oxonium ylide and methane-formaldehyde mechanisms, cannot generate C-C bond from methanol and DME because of very high activation energies

^a Department of Chemistry, inGAP Centre of Research-based Innovation, University of Oslo, P.O. Box 1033 Blindern, 0315 Oslo, Norway

^b State Key Laboratory of Coal Conversion, Institute of Coal Chemistry, Chinese Academy of Sciences, 27 South Taoyuan Road, Taiyuan 030001, China

**Corresponding author, part 1; *Corresponding author, part 2

and unstable intermediates.¹⁹⁻²¹ Thus, the hydrocarbon pool (HCP) mechanism²²⁻²⁴ has been widely accepted to dominate the steady process, and a significant progress has been achieved recently.

Dai and coworkers found that three-membered ring (MR) compounds, dienes, polymethylcyclopentenyl and polymethylcyclohexenyl cations were formed before polymethylbenzenium cations in H-SAPO-34.²⁵ This suggests that aromatics are produced via olefins-based reaction cycle, and then, the aromatics-based cycle may be initiated and quickly dominate the steady process of MTO reaction. The structures of generated carbenium ions depend on the pore systems of zeolite catalysts. Several types of carbenium ions, i.e. polymethylcyclopentenyl,²⁵⁻³⁴ polymethylbenzenium,^{25,30,35-38} and dienyl carbenium^{25,26,39} were recently observed in H-ZSM-5, H-Beta, H-SSZ-13 and H-DNL-6 with ¹³C NMR spectroscopy (see Table 1), UV/Vis spectroscopy and confirmed by theoretical calculations. These carbenium ions have been proved to be the active hydrocarbon species involved in the aromatic-based and olefin-based cycle.²⁵⁻⁴³

(Table 1)

Nevertheless, the debate on the direct mechanism in methanol conversion to hydrocarbons is still going because the HCP mechanism cannot account for the origin of initial HCP species or the formation of the first C-C bond,^{4,19-21} although it gives a reasonable interpretation of the induction period. In addition, the structures, the compositions and the evolution mechanism of HCP species are not clear yet despite that olefins are believed to form through repeated methylation and/or cracking of a pool of hydrocarbons, e.g. aromatics and alkenes trapped inside zeolite catalyst pores in the steady process. The IR and ¹³C MAS NMR results for the conversion of surface methoxy species (SMS) over acidic zeolites support that the initial C-C bond forms via the direct mechanism,^{26,44-46} although the computed energy barriers are unrealistically high and the proposed intermediates are remarkably unstable.¹⁹⁻²¹ Furthermore, organic residuals in the calcined zeolite catalyst or trace amounts of impurities in the methanol and the carrier gas can accelerate the reaction process.⁴⁷⁻⁵⁰ In particular, it was recently identified that initial hydrocarbon species could be directly generated from SMS and DME.⁵¹⁻⁵³ Such inconsistency shows that the issue concerning the origin of the HCP species is still not convincing.

1.2 Previously proposed direct mechanisms

1.2.1 Oxonium ylide mechanism. This mechanism involves the formation of two important intermediates, viz. trimethyl oxonium ion (TMO) and dimethyl oxonium methyl ylide (DOMY) species (Fig. 2). Although TMO was not observed in the reaction of methanol and DME by FTIR and ¹³C solid state NMR spectroscopy on working MTH catalyst,⁵⁴⁻⁵⁶ the formation of TMO is not impossible under MTH conditions since it became appreciable at 347 °C and dominant at 407 °C when pulsing proton-held methanol and DME dimers in an electron beam high pressure ion source mass spectrometer.⁵⁷ With ¹³C cross-polarization magic-angle spinning (CP/MAS) NMR spectroscopy, Hellring and coworkers found that the SMS resonance signal steadily increased at 20 °C at the expense of the TMO signal when trimethyloxonium tetrafluoroborate (TMO⁺BF₄⁻) was added on H-ZSM-5.⁵⁸ In particular, significant

amounts of TMO were generated from DME over H-ZSM-5 at 20 °C.⁵⁹ A further increase in the reaction temperature to 150 °C resulted in the formation of hydrocarbons.

(Fig. 2)

Van den Berg and coworkers suppose that DME molecule interacts with the Brønsted acid site of zeolite to form dimethyl oxonium ions (DMO), which further reacts with another DME molecule to form TMO,⁶⁰ and is subsequently deprotonated one hydrogen by the conjugate base site (ZO⁻) of zeolite to form surface associated DOMY. The species then transforms to methyl ethyl ether (MEE) or ethyl dimethyl oxonium ion (EDMO) via intramolecular Stevens rearrangement⁶⁰ or intermolecular CH₃ transfer,⁶¹ followed by formation of ethene. The rate-determining step is formation of DOMY. However, attempts to detect DOMY failed. Only was MEE detected with CP/MAS NMR together with hydrocarbon species.⁶² The theoretical calculations show that TMO is stable in the H-ZSM-5 framework, but no possible route exists from TMO to DOMY, as the zeolite framework does not offer supplementary stabilization, making it a highly energetic species. Therefore, oxonium ylide mechanism is unlikely to occur in the MTH process.¹⁹⁻²¹ Nevertheless, TMO is a more effective methylating agent than SMS, methanol and DME.⁶³

1.2.2 Carbene mechanism. As shown in Fig. 3, two routes were proposed for carbene mechanism, i.e. α-elimination of water from methanol^{1,64} and decomposition of SMS.⁶⁵ The carbene species polymerize to form olefin or ethanol (EtOH) or MEE by concurrent sp³ insertion into methanol or DME molecule.

(Fig. 3)

Wang and coworkers^{44,66,67} observed the conversion of SMS into hydrocarbons on zeolites, and claimed that the decomposition of SMS may occur via either carbene or oxonium ylide mechanism. However, Sinclair and Lesthaeghe found that the energy barrier for decomposition of SMS were very high (221 kJ/mol on 3T cluster and 244.8 kJ/mol on 41T cluster), and the rate coefficient is as low as $5.3 \times 10^{-7} \text{ s}^{-1}$ at 447 °C.^{20,68} This shows that the possibility for occurrence of carbene mechanism is very small despite that recent IR spectroscopy studies identified the carbene species in the methylation of ethene on H-ZSM-5.^{51,52}

1.2.3 Methane-formaldehyde mechanism. Formaldehyde and methane was mainly observed when converting low-pressure methanol (1-3 Pa) over H-ZSM-5 at 397 °C.⁶⁹ An increase in the methanol pressure to 100 Pa resulted in the formation of hydrocarbons. This leads to the supposition of methane-formaldehyde mechanism, which is also supported by the results obtained by Kubelková and Hutchings⁷⁰⁻⁷⁴ that methane was formed before C₂⁺ hydrocarbons at low methanol coverage. This mechanism includes two steps. One is the reaction of methanol (H⁺ donor) and SMS (methyl donor) to produce initial CH₄ and formaldehyde and regenerate acidic sites in zeolite, as shown in Fig. 4.⁷⁵ Its energy barrier was calculated to be in the range of 148.2 – 189.9 kJ/mol depending on cluster sizes and computational methods.^{19,20,75,76} The other is the C-C coupling of CH₃⁻ generated by back-donating one proton of CH₄ to the zeolite conjugate base oxygen (ZO⁻) and formaldehyde activated by acid site to form EtOH. However, the computational results obtained with different models

all confirm that the energy barrier of this step is high (124.5 to 185.0 kJ/mol) and particularly the reaction rate constant is quite low ($1.2 \times 10^{-7} - 7.4 \times 10^{-1} \text{ s}^{-1}$).^{19,20,53,76} Hence, the methane-formaldehyde mechanism is also difficult to occur although the first step to release methane and formaldehyde is possible.¹⁹

(Fig. 4)

1.3 Is the direct mechanism possible?

Although the decrease of methanol conversion with the increase in methanol purity leads to a conclusion that MTH reaction is started by trace amounts of organic impurities in the methanol, catalyst, and/or carrier gas,⁴⁷ a contradictory result was obtained over SMS-formed H-Y and H-SAPO-34 by the combined ¹³C MAS NMR and diffuse reflectance UV-vis spectroscopy; which shows that the organic impurities (< 30 ppm vs. ca. 1000 ppm) in methanol does not have significant influence on the product distribution.²⁶ Furthermore, it was found that aromatics and carbenium ions could not be detected on H-SAPO-34 in a way similar to that operated in the conversion of SMS when the ethanol and acetone coverage is less than 0.1 molecule per bridging OH group. However, such coverage needs the content of ethanol and acetone as organic impurities to be at least two orders of magnitude higher than that present in the methanol, showing that trace amounts of organic impurities in the methanol does not govern the formation of hydrocarbons from SMS. Thus, the conclusion on the origin of HCP species cannot be drawn yet despite of the fact that the induction period is sensitive to the organic impurities in the feed, catalyst and/or carrier gas.

The IR spectroscopy result shows that CD₃-SMS formed when CD₃OH adsorbed on H-ZSM-5 at 150 °C,⁴⁴ but an increase in the heating temperature led to its decomposition, and the degree increased with the heating temperature. It was found that the C–D band completely disappeared at 239 °C with the formation of ZO-D and hydrocarbons. This is in agreement with the result obtained by Wang and coworkers^{44,66,67} with NMR spectroscopy that the C–H bond activation of SMS may occur at 250 °C under flow conditions. Marcus and coworkers could not detect the C–H activation in the reaction of water and equal amounts of CH₃-SMS and CD₃-SMS because they did not analyse the isotopic distribution in hydrocarbon product but only [D_n]-DME isotopomers which formed via methyl-exchange reaction.⁴⁹ Thus, it can be deduced that the C–H bond activation is related to the direct mechanism of the MTH process and SMS may be a possible intermediate species. Another result worthy of being pointed out is that CD₃-SMS might directly react with ethene to generate propene via formation of carbene-like intermediates, which was recently found by Yamazaki and coworkers⁵¹ with IR spectroscopy and gas chromatography–mass spectroscopy (GC-MS).

Li *et al.* initially compared the reaction behaviour of methanol and DME on a fully calcined SAPO-34 (FC-SAPO-34) catalyst using a pulse reactor.⁵³ It was found that DME is much more reactive than methanol in the original MTH process but the methanol conversion increased at a far higher reaction rate with pulse times (Fig. 5(a)). In particular, no significant effect of HCP species was observed on the promotion of DME conversion. This shows that the conversion mechanism of DME is different from that of methanol. The

methanol conversion follows a typical HCP mechanism, while the conversion of DME occurs via a different route. A further experiment with ¹³C methanol gives only ¹³C olefins on FC-SAPO-34. In contrast, with a mixture of ¹²C and ¹³C methanol as feedstock or non-fully calcined SAPO-34 (NFC-SAPO-34) as catalyst, both ¹²C and ¹³C olefins were obtained (Fig. 5(b)). This suggests that the conversion of DME should occur via a direct route. Indeed, a new direct route for the transformation of DME to hydrocarbons was acquired by combination of IR spectroscopy and theoretical computation results. It will be described in detail later. Since DME can be rapidly formed from methanol, it is possible of the formation of the first C–C bond via the direct mechanism in MTH process over protonated zeolite catalysts.

(Fig. 5)

1.4 Pathway for the direct mechanism

1.4.1 Formation of methoxy groups. SMS is reactive for a number of probe molecules such as water, methanol and aniline. The formation of SMS from adsorbed methanol or DME is the first step of the direct mechanism. Consequently, it has been studied extensively with FT-IR and ¹³C MAS NMR spectroscopy and/or theoretical calculations.^{11,44} It was shown that at least two types of methoxy groups are distinguishable. One type is those formed on the bridging Brønsted acid sites, two characteristic ν(CH) vibration bands of which appear at about 2980 cm⁻¹ and in the range 2868–2850 cm⁻¹ in the FTIR spectra;^{77–80} the other type is those analogous species associated with terminating silanol groups or other defects, which are characterized by the vibration bands at 2959 and 2855 cm⁻¹.^{54,77} The ¹³C chemical shift of methoxy groups most probably centers in the range of 56–60 ppm. This is determined by a wide range of NMR spectroscopy and *ab initio* calculation results⁸¹ by considering peak broadening and mobility differences of methanol and surface bound SMS groups.⁸² Recently, Bhan and co-workers provided further evidence for the existence of SMS by titrating a spent butene and aromatics methylation catalyst surface with water. It desorbed the same amount of methanol as that of framework Al after purging the reaction surface at elevated temperatures.^{83,84}

Upon methanol adsorption on fully calcined SAPO-34, the SMS are readily formed as the first intermediate species.⁵³ This can be seen by the gradual shift of the asymmetric C–H stretching vibration band of chemisorbed methanol from 2958 to 2977 cm⁻¹ with the increase of temperature from 50 to 300 °C (Fig. 6(a)). Regardless of this, the chemisorbed DME cannot be transformed into the SMS at low pressure because most of the DME is desorbed upon evacuation and increase of temperature due to its very low adsorption energy (33.8 kJ/mol) on zeolite catalysts (Fig. 6(b)). SMS could only be formed from DME when its pressure was higher than 12 Pa (Fig. 6(c)).⁵³

(Fig. 6)

It is worth pointing out that the results recently obtained by Iglesia and coworkers by pulsing DME into a continuous flow fixed bed reactor at low temperature also support the formation of surface bound SMS species.^{80,85–87} The adsorption amounts of DME on H-ZSM-5, H-FER and H-MOR are all very close to 0.5 molecules per Al

atom, in agreement with the quantities of generated water molecules and SMS species.

Despite that the formation of SMS from adsorbed methanol and/or DME has been definitely proved by IR and ^{13}C MAS NMR spectroscopy; detailed pathways can only be attained by theoretical computations in the present time because of the spectroscopic and experimental limits. Up to date, several routes were proposed for formation of SMS from methanol or DME (Fig. 7).⁵³

(Fig. 7)

A typical unassisted route is shown in Fig. 7(a). First, one methanol (or DME) molecule physically adsorbs on the Brønsted acid site in an end-on manner through hydrogen bonding. Then, the Brønsted proton moves to the O anion of methanol or DME, forming a transition structure with the C-O bond of methanol (or DME) being weakened and elongated. Finally, the SMS is generated by eliminating a water (or methanol) molecule. As for the assisted route, the primary difference from the unassisted one is that two methanol (or DME) molecules physically co-adsorb on one Brønsted acid site in the end-on manner via the hydrogen bonding (Fig. 7(b)).

The earlier calculation results obtained with small cluster models (3T, 5T and 8T) show that the transition state for formation of SMS can be stabilized by another methanol molecule by decreasing enthalpy barrier. However, this stabilization effect was contradicted by the result attained with a large cluster model (46T, $\omega\text{B97X-D/6-31g(d,p)}/\text{ONIOM(B3LYP/6-31g(d,p):MNDO}$).⁸⁸ The enthalpy barrier slightly changes in the range of 129 – 133 kJ/mol for both the unassisted and assisted routes. This is further confirmed by the result obtained with periodic model (VASP) that the energy barriers for formation of SMS from methanol over H-SAPO-34 in the assisted route is 138 kJ/mol (Fig. 8),⁵³ and the rate constants are 9.0×10^{-2} and $1.7 \times 10^{-2} \text{ s}^{-1}$ at 250 and 400 °C respectively. This indicates that the stabilization effect of zeolite framework is much more significant than the electrostatic stabilization induced by the assisting methanol. Fig. 9 shows that ringlike transition states are formed in the assisted route, which results in an increased entropy loss and higher free-energy barrier.

(Fig. 8 & 9)

Another route for formation of SMS from methanol or DME is a stepwise pathway. Two DME molecules first react with Brønsted acid to form methanol, TMO and ZO^+ .⁵³ TMO then rapidly dissociates to SMS and DME. The energy barrier and rate constant at 400 °C of the first step are 101 kJ/mol and $1.3 \times 10^4 \text{ s}^{-1}$,⁵³ while those of the second step are 60 kJ/mol and $1.9 \times 10^{10} \text{ s}^{-1}$.

All the cluster models invariably show that the formation of methoxy groups from methanol or DME is an endothermic reaction, which is in the range from +43 to +57 kJ/mol.¹¹ Employing sophisticated ONIOM methods and periodic models gave similar values, being +66 kJ/mol and +75 kJ/mol,^{53,89} which are zero point vibrational energy (ZPVE) corrected electronic energies.

In this context, metadynamics simulation method was used to study the formation pathway of SMS.⁸⁸ This method gave higher free-energy barrier for pathway from methanol than from DME in the unassisted route maybe due to the consideration of conformational entropy. The metadynamics simulation also shed a different light on

the assisting effect of methanol molecule. A lower free-energy barrier was obtained for the formation of SMS from methanol in the assisted route than the unassisted one,⁸⁸ while no difference was observed for the reaction from DME. This demonstrates that the proton transfer from the zeolite to the guest molecules is almost finished before the formation of SMS, mitigating the entropic penalty of the ringlike transition structure obtained in the static calculations.⁸⁸ This shows that the formation of SMS is governed by many factors, and ultimately dependent on the precise reaction conditions. Co-adsorption of another methanol molecule may result in an increase of adsorption enthalpy but cause an additional entropy loss. At typical reaction temperature, the entropic penalty mitigates the enthalpic stabilization, resulting in a positive free energy of adsorption. Regardless of this, molecular dynamics simulations provided insights into the kinetic and thermodynamic stability of the complexes considering the large entropic contributions.

1.4.2 A possible route for formation of initial C-C bond. Recently, a combination of experiment and DFT calculation results led to a possible direct route for formation of initial C-C bonds over H-SAPO-34.⁵³ This direct route involves the formation of methoxymethyl cation ($\text{CH}_3\text{OCH}_2^+$) intermediates from SMS and DME (Fig. 10) despite that methane is simultaneously formed. The methoxymethyl cation further couples with another DME or methanol molecule to form C-C bond-containing 1,2-dimethoxy ethane or 2-methoxyethanol, which gives propene as initial alkene product through the formation of a series of oxonium cations via methylation, deprotonation, dealkylation, H-shift and elimination. It was found that propene, not ethene, induced the occurrence of the HCP mechanism. The energy barriers calculated with periodic model of the first step and the second step are 135 and 95 kJ/mol (for 1,2-dimethoxy ethane) or 102 kJ/mol (for 2-methoxy ethanol), and their rate constants at 400 °C are 4.2×10^4 and $2.4 \times 10^5 \text{ s}^{-1}$ (for 1,2-dimethoxy ethane) or $3.7 \times 10^5 \text{ s}^{-1}$ (for 2-methoxy ethanol), respectively (Fig. 11). To our knowledge, this is the most energetically favoured route reported for the formation of the first C-C bond (Table 2). It is worth noting that the coupling reaction of methoxymethyl cation and methane to form ethanol is also possible although its energy barrier (125 kJ/mol) is higher than the reaction of methoxymethyl cation and DME by 30 kJ/mol, because its rate constant is $1.3 \times 10^1 \text{ s}^{-1}$ (400 °C). Since all of these calculated energy barriers include zero point vibrational energy (ZPVE) correction, the much lower rate constant of the reaction of methoxymethyl cation and methane can be attributed to the much larger entropy loss of methane. This indicates that the entropic contribution of methane is significant, and it prefers to desorb and diffuse into gas phase rather than further coupling with methoxymethyl cation.

(Fig. 10 & 11, Table 2)

The structures of initial, transition and final states of the two steps in the methoxymethyl mechanism are shown in Fig. 12. The transition states for the coupling of methoxymethyl cation with DME, methanol and methane are similar, but the coupling with DME is the most energetically favorable pathway. Nonetheless, the rate-determining step is the formation of methoxymethyl cations. The high stabilization energy of $\text{CH}_3\text{OCH}_2^+$ species (276 kJ/mol relative to CH_3^+)⁹⁰ in the CHA cavity of SAPO-34 enables detection

by in situ IR spectroscopy by carefully controlling the conditions of the reaction of DME and SMS.⁵³ Indeed, when 6.5 Pa of DME was introduced into the IR cell equipped with SMS-formed FC-SAPO-34 self-supported wafer, an increase in the temperature from 30 to 180 °C led to the appearance of a new band at 2960 cm⁻¹, which is characteristic of asymmetric C-H stretching vibration of CH₂ group in CH₃OCH₂OZ (Z = zeolite) (Fig. 13).⁹¹ Natural Resonance Theory (NRT) analysis⁹² at MP2/cc-pVQZ level reveals that 95.27% of the methoxymethyl cations exist in the form of H₂C=O⁺-CH₃, while only 0.40% is present as carbenium ion (H₂C⁺-O-CH₃) (Fig. 14, unpublished result). This is supported by the successful preparation of H₂C=O⁺-CH₃ species in superacidic media.⁹³

(Fig. 12 – 14)

The formation of methoxymethyl cations was further confirmed by the results obtained in the reaction of DME over D₃-SMS-formed FC-SAPO-34. It was found that the molar ratio of CH₃OCH₃(I): CH₃OCD₃(II): CD₃OCD₃(III) in the effluent was about 55: 34: 11.⁹⁴ This supports that the methyl exchange reaction of SMS and DME occurs via the formation of TMO. The product contains five types of isotopic methane, i.e. CH₄, CH₃D, CD₃H, CD₄ and CH₂D₂. The much higher content of CH₄ (49%), CH₃D (15%), CD₃H (21%) and CD₄ (12%) than CH₂D₂ (3%) indicates that methane is formed through the reaction of methyl group of CH₃-SMS or CD₃-SMS and hydrogen (H) or deuterium (D) of [D_n]-DME (n = 0, 3 or 6). This not only accounts for the methane formation mechanism, but also gives another piece of evidence for the formation of methoxymethyl cations.

Nonetheless, the direct formation of 1,2-dimethoxy ethane or 2-methoxyethanol from methoxymethyl cations and DME or methanol has not yet been experimentally validated although it is demonstrated by the theoretical calculation result. Validation requires kinetic isotope effect (KIE) studies and operando spectroscopy analysis, which are now in progress.

Part 2:

Catalyst deactivation by (hydro-)carbon residues

2.1 Thermodynamic considerations

In this section, we will consider deactivation by (hydro-)carbon residues, that is; any carbon-containing compound which has too low vapor pressure, too high proton affinity, or is too spacious, to leave the surface (internal or external) of a catalyst. The compounds may be graphitic, aromatic or polymeric in nature. Before considering experimental findings from MTH studies, it is useful to revisit the thermodynamic driving force leading to the formation of various types of carbon-containing deposits under typical MTH conditions. Fig. 15 shows the Gibbs energy of formation per carbon atom for methanol and some selected alkane, alkene, aromatic and polyaromatic compounds, as well as amorphous carbon and water. The thermodynamic data were found in⁹⁵. The more stable molecules are found lowest on the Gibbs energy per C atom scale, and the thermodynamic driving force of intermolecular reactions may easily be found by comparing the Gibbs energy per C atom for the product molecules and reactant molecules involved.

(Fig. 15)

When methanol is converted to hydrocarbons, one water molecule is formed per carbon molecule converted (Eq. 2.1). Therefore, Fig. 15 contains the Gibbs energy of methanol minus the Gibbs energy of water to illustrate the release of energy associated with the main MTH reaction (Eq. (2.1)).

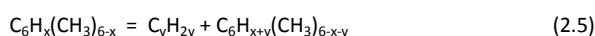
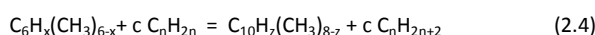
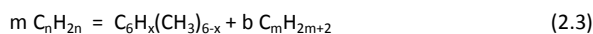


Fig. 15 clearly shows that all methylation reactions by methanol are thermodynamically favored throughout the temperature range associated with the MTH process, thus creating a thermodynamic drive for complete methanol conversion. When considering the data for hydrocarbon inter-conversion reactions, a comparison between the Gibbs energy of formation per C atom for propene and 2-methyl-1-pentene, respectively, shows that propene dimerisation (Eq. (2.2)) is favored only at temperatures below 370 °C. The thermodynamic driving force for C₆= cracking rather than C₃= dimerization at temperatures above 370 °C suggests that polyalkene type coke will not be formed under typical MTH conditions. Turning the attention to arene formation, which proceeds through a “disproportionation” of alkenes to arenes and alkanes (Eq. (2.3)), Fig. 15 shows that all considered aromatic molecules, as well as the corresponding alkane, are more thermodynamically favored than the corresponding alkene in the complete temperature range considered, suggesting a strong thermodynamic drive for arene (and alkane) formation. Furthermore, the bicyclic arene, naphthalene, is thermodynamically more favored than the monocyclic arenes (represented by benzene and trimethylbenzene) at temperatures higher than 360 °C. Conversion of an aromatic monocycle into an aromatic polycycle requires a hydrogen acceptor, e.g. alkene to alkane conversion (Eq. (2.4)). As commented above, such hydrogenation is favorable under typical MTH conditions. Together, these two transformations represent a strong thermodynamic driving force for the formation of polycyclic arenes under typical MTH conditions.

Although the main focus of this section is deactivation, the thermodynamic treatment of the MTH reaction would not be complete without considering a competing reaction to polycyclic arene formation, i.e., the dealkylation of polymethylated benzene to form an alkene and a less methylated benzene analogue (Eq. (2.5)). This reaction is an important part of the dual-cycle mechanism (Fig. 1). Considering again Fig. 15, it is clear that the dealkylation reaction is less favored than polycyclic arene formation. However, the reaction becomes more thermodynamically favored with increasing temperature. Furthermore, alkene formation does not require the presence of a hydrogen acceptor.

The ultimate coke compound is carbon. By definition, the Gibbs energy of formation for graphitic carbon is zero. As shown in Fig. 15,

the Gibbs energy of formation for amorphous carbon is also lower than for any hydrocarbon considered here. This means that all those hydrocarbons may ultimately be transformed to carbon under MTH conditions, provided the residence time is long enough.

2.2 Experimental observations of (hydro-)carbon residues

Thermogravimetric analysis (TGA) is the classical tool in catalyst deactivation studies. The amount and composition of (hydro-)carbon residues may be determined by monitoring the weight change as well as the C:H ratio in products detected by on-line mass spectrometry, respectively, during Temperature-Programmed Oxidation (TPO) of the used catalyst (see e.g. ⁹⁶). However, TGA gives limited information about the nature of (hydro-)carbon residues, and the introduction of the "Guisnet method" by Guisnet and coworkers in the late 1980ies represented a major breakthrough in deactivation studies of zeolite and zeotype catalysts.⁹⁷ In this method, the zeolite or zeotype lattice is dissolved in hydrofluoric acid, followed by extraction of the unaltered hydrocarbon residues in di- or tetrachloro-methane and analysis of the extract by GC-MS. Since the 1990ies, other ex-situ and in-situ/operando methods have gradually been introduced. The aim is to monitor the formation (and depletion) of active pool species, deactivating species and coke during the MTH reaction. Such methods include NMR²³, UV-VIS⁹⁸, IR⁹⁹, fluid bed Raman¹⁰⁰ and EPR¹⁰¹ spectroscopy, TEOM¹⁰², LDI-TOF MS¹⁰³, Confocal fluorescence microscopy and UV-VIS micro-spectroscopy⁹⁸.

In MTH, the term "deactivating species" is not unambiguous. As an example, let us consider three zeolites and zeotypes that represent the three main varieties of active hydrocarbon pool species in the "dual cycle" mechanism (Fig. 1): H-ZSM-22 (TON structure, 1D, 10-ring, pore size $4.6 \times 5.7 \text{ \AA}^2$), H-ZSM-5 (MFI structure; 3D, 10-ring, pore sizes 5.1×5.5 and $5.3 \times 5.6 \text{ \AA}^2$) and H-SAPO-34 (CHA structure, 3D, 12-ring cavities and 8-ring windows, window size $3.8 \times 3.8 \text{ \AA}^2$). The pore structure of the three topologies is shown in Fig. 16. Transient studies have shown that H-ZSM-22 catalyzes methanol conversion via the alkene cycle, while aromatic species formed in this catalyst are largely inert towards alkene formation and are also trapped in the zeolite structure.¹⁰⁴ Similar studies of H-ZSM-5 further showed that this zeolite catalyzes methanol conversion to a similar extent via the alkene and arene cycle, and that the activity of the aromatic pool species decreases with an increasing number of methyl groups on the polymethyl benzene intermediates.¹⁰⁵ Finally, transient studies of H-SAPO-34 showed that this catalyst converts methanol mainly via the arene cycle, and that the most substituted polymethylbenzene, hexamethyl benzene (hexaMB) is the most active pool species in this topology.^{106, 107} Together, these three studies suggest that a hydrocarbon which is an active pool species in one catalyst topology (such as hexaMB in CHA) may be a deactivating species in another topology (such as TON). The term "deactivating species" could also include species which are active for alkene formation, but have a higher proton affinity as well as distinctively lower activity than other pool species. Such species will tend to occupy the active sites and thereby contribute to an overall lower methanol conversion. In that context, hexaMB might be considered a deactivating species even in the MFI structure.

Considering larger species, studies of methylated naphthalenes have shown that they may undergo dealkylation reactions similar to those of polymethyl benzenes, however at a much lower rate.^{108, 109} Therefore, bi- and polycyclic arenes may be considered deactivating species in any MTH catalyst.

The Guisnet method is still the only method which identifies and distinguishes individual molecules in a used zeolite or zeotype catalyst. A few examples of hydrocarbon residues detected by the Guisnet method in the same three zeolites and zeotypes discussed above; i.e., H-ZSM-22, H-ZSM-5 and H-SAPO-34, are shown in Fig. 17 and Fig. 18.

We will first consider the total ion chromatograms observed after testing H-ZSM-22 for different times on stream at 400 °C (Fig. 17). Already after 5 min on stream, the catalyst contained significant amounts of alkyl benzenes, which may barely leave the catalyst.¹¹⁰

(Fig. 17)

With increasing times on stream, the amount and size of hydrocarbon deposits increased. After 5 h on stream, when the catalyst was severely deactivated, it contained mono-, di- and tricyclic arenes. This time evolution is in line with the expectations from thermodynamic considerations (Fig. 15). The hydrocarbon deposits observed in severely deactivated H-ZSM-5 and H-SAPO-34 are shown in Fig. 18. As expected from its cavity-window structure, H-SAPO-34 contained high amounts of arene deposits, with 1 - 4 aromatic rings, after testing. On the other hand, H-ZSM-5, which has slightly larger pore size than H-ZSM-22, contained only monocyclic arenes in detectable amounts after testing. The latter observation is probably related to a combination of the low, but significant rate of dealkylation of even hexamethyl benzene in H-ZSM-5¹⁰⁵, combined with its excellent diffusion properties: In a recent contribution, Beato et al studied hydrocarbons retained in H-ZSM-5 by in-situ Raman spectroscopy during methanol conversion at 350 °C. When the catalyst was flushed with inert gas after testing, they observed that aromatic species were rapidly depleted in the H-ZSM-5 crystal.¹⁰⁰

(Fig. 18)

The difference in the tendency of forming polymethylated and polycyclic arenes between H-ZSM-22, H-ZSM-5 and H-SAPO-34 is mirrored by their deactivation rates. While keeping in mind that other parameters than catalyst topology were simultaneously varied in those studies, it is interesting to note that H-ZSM-22 and H-SAPO-34 have been reported to yield similar methanol conversion capacity per acid site.¹¹⁰ On the other hand, a comparison between H-ZSM-5 and H-ZSM-22 suggested that H-ZSM-5 had 20 times higher methanol conversion capacity than H-ZSM-22.¹¹¹ More direct evidence for an inverse correlation between catalyst stability and the catalyst's tendency of forming polyarene compounds was found in two recent studies of catalysts with similar pore size and dimensionality, but with different intersection or cavity sizes. In the first study, four 3D 10-ring zeolite materials with similar crystal size, acid strength, and acid site density but varying topologies were compared at 350 °C.¹¹² Two of the zeolites, H-ZSM-5 (MFI) and H-ZSM-11 (MEL), have small channel intersection volumes, and the two others, H-IM-5 (IMF) and H-TNU-9 (TUN), have extended channel intersections. All materials have

similar channel sizes, and a very similar effluent product distribution was reported for the four samples. However, the topologies with larger intersections deactivated much more rapidly than those with smaller intersections. Moreover, the topologies with extended channel intersections contained much more, and heavier, hydrocarbon residues, thus clearly demonstrating the correlation between topology and deactivation owing to sterically demanding molecules formed in internal cavities. In another study, four topologies with 8-ring windows and varying cavity sizes, H-SAPO-34 (CHA), UZM-12 (ERI), UZS-9 (LTA), and UZM-5 (UFI), were compared as MTH catalysts at 350 °C.¹¹³ Also here it was observed that the topologies that deactivated more rapidly contained heavier polycyclic arenes after testing than those that deactivated less rapidly.

Other parameters which have been reported to contribute to more rapid deactivation by hydrocarbon deposition are higher acid strength, higher acid site density and larger crystal size.^{4, 114-120} All three observations could simply be the effect of an alteration of the relative diffusion and reaction rates in the crystals, resulting in a larger fraction of secondary reactions before products may diffuse out to the gas phase. However, material properties could also alter the preferred reaction paths. Westgård Erichsen et al recently performed a comparative study of H-SAPO-5 and H-SSZ-24 catalysts for the MTH reaction. Both materials have AFI topology, but different acid strength. For all conversions, it was found that the more acidic H-SSZ-24 yielded much higher selectivities to arenes than the less acidic H-SAPO-5, thus suggesting that a higher acid strength favors intermolecular hydride transfer reactions.¹⁸

2.3 Time evolution of (hydro)-carbon deposits at the micro- and meso-scale

The two commercial MTH catalysts, H-ZSM-5 and H-SAPO-34, are by far the most extensively studied catalysts for the title reaction, also with regards to catalyst stability. H-beta zeolite (3D, 12-ring, 7.1×7.3 and 5.6×5.6 Å² pore dimensions) probably comes on a third place, mainly because its pores are large enough to allow for model studies of polymethylated arenes (benzene, naphthalene), alkenes and methanol. Here, we shall start with referring a few such model studies, and then proceed to recent studies covering the evolution of (hydro)-carbon deposits and deactivation of H-ZSM-5 and H-SAPO-34 catalysts.

2.3.1 Model studies. Sassi et al. fed pulses of (poly-)methylated benzene and methanol over H-Beta zeolite at 450 °C and observed the formation of higher methylated benzene, as well as ethyl- and isopropyl-substituted analogues in the reactor effluent. They further observed small amounts of tetrahydromethylated naphthalene and suggested that the second ring of this molecule was formed by coupling of two isopropyl substituents in ortho position.³⁶ Later, Bjørgen et al. fed a constant stream of hexamethyl benzene (hexaMB) over H-Beta zeolite at 325 °C. They analysed the hydrocarbons retained in the zeolite after quenching by using the Guisnet method and observed that dihydrotrimethylnaphthalene was the first bicyclic compound formed. They suggested that the bicyclic product was formed by rearrangement of the heptamethyl benzenium ion, which is an important intermediate even in the dual

cycle mechanism (See. Fig. 1). The conclusion was supported by co-feed studies of ¹³C-methanol and ¹²C-naphthalene.¹²¹

More recently, Bjørgen et al. extended the mechanistic studies to co-feeding ¹³C-methanol and ¹²C-benzene over three 12-ring topologies (H-beta, H-MCM-22, and H-mordenite). They reported that trimethylnaphthalene was the smallest bicyclic compound formed in all topologies, pointing to Hepta MB⁺ rearrangement as a major formation pathway. However, they further observed that the bicyclic compounds formed during deactivation contained a higher fraction of unlabeled carbon than the heptaMB⁺ ion, thus pointing to a more complex mechanism of polycyclic arene formation.¹²²

2.3.2 Case study 1: H-ZSM-5. A recent contribution by Schulz constitutes a reference point for current deactivation studies of H-ZSM-5.¹²³ Schulz reported that catalytic tests performed using H-ZSM-5 at temperatures below 300 °C led to rapid activity loss and significant hydrocarbon deposition compared to tests employing the same catalyst at higher temperatures. At 290 °C, the catalyst lifetime was 0.5 h, and the catalyst contained 10 % (hydro)-carbon deposits after testing. At 380 °C, the lifetime increased to 400 h, and the catalyst contained only 0.3 % (hydro)-carbon deposits after testing. Schulz subjected the catalyst to Temperature-Programmed Desorption after testing at 290 °C, and observed desorption of alkenes and lighter polymethylated benzenes at temperatures above 350 °C. He allocated these observations to a shift in the polymethyl benzene alkylation – dealkylation equilibrium towards the dealkylation side with increasing temperatures, in agreement with the thermodynamic data in Fig. 15. Schulz further suggested that deactivation of H-ZSM-5 is caused by internal hydrocarbon deposits at temperatures below 350 °C, and by external coke at temperatures above 350 °C.

In line with this, Bjørgen et al found no correlation between soluble hydrocarbon deposits (Fig. 18) and deactivation of H-ZSM-5 at 370 °C, and suggested that deactivation was caused by external coke.¹⁷ More recently, Weckhuysen et al applied UV-VIS micro-spectroscopy and confocal fluorescence spectroscopy to monitor the evolution of hydrocarbon deposits in (100×20×20 microns) crystals of H-ZSM-5 at 390 °C. They observed that coke deposition proceeded faster on the triangular edges of the crystals, where straight channels are open to the surface. They further observed that coke formation progressed from the outer sections of the crystals and inwards towards the bulk of the crystal (Fig. 19). An hour-glass pattern was observed in some cases, suggesting diffusion limitations or channel mismatch between the subunits of the crystal.⁹⁸ In a follow-up contribution, they compared several H-ZSM-5 crystals at two temperatures (350 and 500 °C) and reported that increased acid site density (Si/Al < 17) and increasing temperature led to faster transformation of reactive species to polyaromatic coke molecules. Use of polarization-dependent UV-VIS spectroscopy further revealed that the sinusoidal pores contained predominantly small aromatic species, while the straight pores of the crystal contained a significant fraction of polyaromatic molecules. This observation led the authors to conclude that formation of large coke species proceeds by gradual growth in the straight channels, eventually reaching and covering the external

surface of the H-ZSM-5 crystal.¹¹⁸ These findings are generally in line with those of Schulz.¹²³

(Fig. 19)

Very recently, Lercher et al published an in-depth study of the deactivation of H-ZSM-5 in PFR and CSTR reactors at 450 °C (see also Section 2.4.3)¹⁰¹. Characterization of used catalyst from the CSTR reactor using EPR and IR spectroscopy, LDI-TOF MS, TPO and N₂ physisorption, showed that the number of Brønsted acid sites (BAS) decreased with time on stream, while the number of Lewis acid sites (LAS) was retained after testing. Thorough procedures further showed that the deposits covering the BAS were not volatile, and that all uncovered BAS were accessible for pyridine adsorption after testing. The authors therefore concluded that hydrocarbon deposits deactivated the catalyst by poisoning individual sites in the catalyst, and not by hindering access to the catalyst pores by external coking, even at this high temperature. Comparisons of LDI-TOF mass spectrometry of used catalyst particles and hydrocarbon deposits released by using the Guisnet method, respectively, showed that internal deposits were formed before external deposits, and furthermore that the internal deposits were separated by mass units of 12 and 14, suggesting growth by Diels-Alder as well as methylation reactions. External deposits grew mainly by 12 mass units, thereby suggesting a Diels-Alder type mechanism.¹⁰¹

Irrespective of the coke origin, high external surface area and short diffusion pathways are attractive options to reduce deactivation by hydrocarbon deposition (See Section 2.2). For desilicated, hierarchical MFI materials, an increased catalyst lifetime is frequently reported.¹²⁴⁻¹²⁹ This appears to be accompanied by a general shift towards heavier products^{124,126,128,129} and a shift in aromatics distribution towards heavier aromatics.^{124,130} A higher coking tolerance for such treated catalysts has been observed,¹³⁰ as well as a higher propene selectivity in MTP application.¹³⁰ For nanosheet type MFI catalysts, it has similarly been reported that the nanosheet morphologies of H-ZSM-5 give substantial improvements in deactivation resistance.^{131,132} However, the underlying reasons for the improved deactivation resistance are not yet satisfactorily described. Improved diffusion properties and easy desorption of coke precursors as well as a higher coking tolerance are often claimed, but seldom actually demonstrated. Importantly, in a fundamental kinetic study, Hill et al.⁸⁴ demonstrated that there is no difference in the activity per site in the methylation of benzene and toluene when comparing microporous and mesoporous (self-pillared pentasil) catalysts. This strongly indicates that textural properties rather than modifications of the intrinsic reactivity of the individual sites dictate the catalytic behavior of these hierarchical materials.

2.3.4 Case study 2: H-SAPO-34. Studies of the MTH reaction over H-SAPO-34 have revealed that deactivation is accompanied by a gradual transformation of active polymethyl benzenes to less active polycyclic arenes with time on stream; the largest observed species being pyrene.^{107,133-135} The polyaromatic species were initially considered the origin of deactivation. A recent study, which was based on a combination of ¹²C/¹³C transient experiments at 350 °C and studies of retained hydrocarbons by the Guisnet method,

however revealed that catalyst deactivation started before significant formation of polycyclic arenes was observed. They further showed that polycyclic arenes continued to form even after the catalyst was completely deactivated.¹⁰⁷ The results suggested that deactivation was initiated by formation of branched alkanes and alkenes which were trapped in the catalyst cavities, thereby hindering diffusion and enhancing polycyclic arene formation. They further suggested that polycyclic arenes were formed predominantly from methanol and product molecules which were trapped inside deactivated catalyst crystals. Finally, quantification of retained hydrocarbons suggested that only a small fraction of the H-SAPO-34 crystals were taking part in alkene formation. The authors therefore suggested that the MTH reaction mainly took place in the outer parts of the catalyst crystals.¹⁰⁷

A study of the temperature influence for the MTH reaction over H-SAPO-34 revealed a similar effect of temperature as that previously reported for H-ZSM-5¹²³: Bleken et al.¹³⁶ reported that the amount of hydrocarbon residues observed by TPO after 25 min testing decreased from 16% to 6% with increasing test temperature in the temperature range 300 – 400 °C. Furthermore, the retained hydrocarbons observed after 25 min on stream shifted from 70% bicyclic and 30% monocyclic arenes at 300 °C, to 30% bicyclic and 70% monocyclic arenes at 400 °C. The methanol conversion capacity of the H-SAPO-34 catalyst increased from 1 to 22 g methanol per gram catalyst in the same temperature range.

Parallel studies using confocal and micro-spectroscopy techniques on large (50×50×50 microns) crystals of H-SAPO-34 at 260 – 480 °C showed rapid formation of aromatic compounds, which went through a maximum with increasing temperature. The spectra further suggested that monocyclic arenes were gradually transformed to polycyclic arenes and graphitic coke. It was further observed that arenes were first formed at the crystal corners, then at the edges, before progressing towards the crystal core.⁹⁸ Very recently, Qian et al applied a combination of operando UV/Vis and IR spectroscopy, with on-line MS measurements. The set-up allowed for simultaneous detection of retained (aromatic) and effluent (alkene) products.³⁹ During temperature-programmed MTH, product formation was observed between 300 and 400 °C. Methanol, methoxy and protonated dimethyl ether were the main species observed in the catalyst during the induction period. During the product-forming period, polyalkylated benzene carbocations and polyaromatic carbocations were observed in addition to methoxy species. The authors observed that the rates of alkene (represented by propene) and deactivating polycyclic arene formation resembled each other at each temperature, and suggested that the two competitive routes are based on the same reactants, i.e.; methoxy species and polymethyl benzenes.

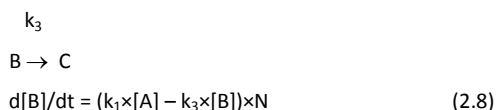
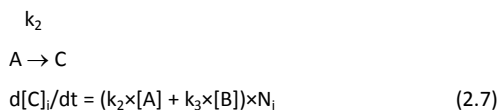
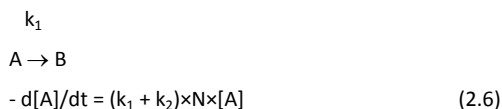
2.4 Time evolution of (hydro-)carbon deposits at the macro-scale

As a general rule, comparisons of catalyst stability should be carried out at less than 100 % initial conversion, to allow a straightforward distinction of catalyst activity and catalyst stability. Studies of single reactions in zeolites, such as alkene and arene methylation reactions, naturally follow this rule. However, when the purpose of the study is to elucidate the life-time performance of a catalyst for

the MTH reaction as such, the situation changes: For an autocatalytic reaction like MTH, stability studies performed at less than 100 % initial conversion in a plug flow reactor (which is the most commonly used reactor type in laboratory scale studies) may imply that only the last fraction of the catalyst bed is catalyzing the autocatalytic reaction, whereas a significant first fraction is catalyzing the much slower initiation reaction. The relative activity of two catalysts may be different for the initiation and autocatalytic reactions, respectively, further complicating data analysis. In conclusion, it has become the norm to perform stability tests of MTH catalysts at full initial conversion, to minimize the impact of the initiation zone.

The difficulty in performing reliable comparisons of MTH catalyst performance, in particular when comparing contributions from laboratories that employ different test protocols, constitutes a significant obstacle to the further advancement of the field. In this section, we will review the current state-of-the-art of quantitative comparisons of catalyst stability for the MTH reaction. Furthermore, we will consider possible sources of deactivating species in different parts of the catalyst bed in a plug flow reactor (PFR). As an introduction, some general characteristics of catalyst deactivation profiles will be presented.

2.4.1 Theoretical profiles for catalyst activity and deactivation. In a general case, coke may be formed directly from the reactant(s), from the product(s) or from both. The coke origin will lead to different deactivation profiles. Fig. 20 shows typical deactivation profiles for the following reaction system, when assuming a reactor with excess catalyst, i.e. 100 % initial conversion:



where A is the reactant, B is an effluent product, C is a deactivating species (coke) and N is the number of active sites. For simplicity, all reaction rates are assumed to show a first order dependence in the reacting species. The concentrations of A and B were integrated over the length of the reactor (100 segments), while C and N in each segment (i) were integrated with time on stream (j):

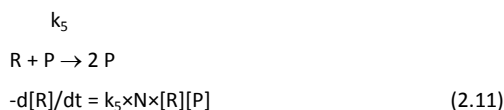
$$N_{i,j} = N_{i,j-1} + C_{i,j} \quad (2.9)$$

where i is the reactor segment and j is the time on stream.

(Fig. 20)

The data in Fig. 20 show that the coke origin may be hypothesized by looking at the shape of the deactivation profile: If coke is mainly formed from the reactant, then the deactivation curve will take an inverse S form, with rapid deactivation after break-through of the reactant. Coke formation mainly from the product will lead to a deactivation curve which slope decreases with time on stream, as the product concentration decreases. An intermediate behavior occurs when both reactant and product are contributing to coke formation.

During the MTH reaction, an additional complexity relates to the autocatalytic nature of this reaction. In an autocatalytic reaction, the rate of reaction between the reactant (R) and a product (P) to form another product (P), Eq. (2.11), is much faster than the rate of reactant conversion alone, Eq. (2.10), in general terms:



where N is the number of active sites and $k_5 \gg k_4$

At a given point in time, when assuming homogeneously distributed active sites throughout the PFR catalyst bed, the conversion versus contact time plot for an autocatalytic reaction generally takes an S form, with a gradual transition from the initiation zone where the autocatalytic species is slowly formed, to the autocatalytic zone where the autocatalytic reaction dominates, and finally to the reactant depletion zone where full conversion is reached (Fig. 21). The slopes and transition points between the zones depend on the absolute and relative values of k_4 and k_5 .

(Fig. 21)

The reaction profile in Fig. 21 suggests that the catalyst bed may be divided into three zones with distinctively different gas phase composition when the MTH reaction is carried out in a PFR with full initial conversion:

1. The initiation zone, where methanol is converted to dimethyl ether (DME) and further to hydrocarbons (and water). This zone is characterised by a high concentration of oxygenates and a low concentration of hydrocarbons.
2. The autocatalytic zone, where oxygenates and hydrocarbons exist side by side and product formation is dominated by the autocatalytic reaction, and
3. The product zone, where methanol is depleted and hydrocarbon inter-conversion reactions dominate.

A schematic view of the three zones is shown in Fig. 22.

(Fig. 22)

Experimental product yield versus methanol conversion plots for various MTH catalysts are shown in Fig. 23. With all catalysts, it is observed that for methanol conversions in the range ~10-80 % (the autocatalytic zone), product selectivity is remarkably independent of conversion. In the subsequent product zone, product selectivity changes with conversion as methanol is gradually depleted.

(Fig. 23)

2.4.2 Towards quantitative comparisons of catalyst stability. Early kinetic models of the MTH reaction were aimed at describing the life-time performance of a given catalyst under various process conditions (see ⁵ and ref.s therein). Recently, Janssens targeted another ambition: To enable quantitative comparisons of catalyst stability by an analytical solution of the mathematical expression for (hydro-)carbon deposit formation during reaction.¹³⁷ Janssens described catalyst deactivation as a reduction of the effective amount of catalyst in the reactor with time. The approach was based on the observation that the changes in product distribution over H-ZSM-5, especially an enhanced yield of propene and ethene shortly before the breakthrough of methanol, resembles the development of the product distribution which is expected with a continuously increasing space velocity.¹³⁸ To calculate the conversion with time on stream, it was assumed that the MTG reaction is first order in methanol, and that the deactivation rate is proportional to the conversion, which corresponds to a constant selectivity for coke formation. Further support for such an assumption was found in the literature: First, reported conversion versus time on stream curves generally follow an inverse S shape,^{5,37,123,137-143} in accordance with the parallel coke formation model in Fig. 20. Second, several authors reported that visual inspection of the catalyst bed after testing of H-ZSM-5 or H-SAPO-34 catalysts at 350 °C or higher showed a coked zone starting at, or shortly below, the entrance of the reactor, while the last part of the catalyst bed was still white or light grey, as illustrated in Fig. 24.^{123,144-146}

(Fig. 24)

These visual inspections further supported that methanol is a main source of hydrocarbon deposit formation. With these assumptions, Janssens found that for a catalytic test starting with full methanol conversion, the ratio of the catalyst life time to 50% yield of hydrocarbons and the applied contact time (W/F weight-to-flow ratio) is a direct measure for the deactivation rate, independent of the activity.¹³⁸ The model was later successfully applied to relate the deactivation of a large number of H-ZSM-5 based catalysts with the presence of internal silanol groups inside the zeolite channels.¹⁴⁷

Clearly, a model like that suggested by Janssens has certain limitations. One limitation is related to catalyst selectivity: Catalyst deactivation can only be considered simply as a loss of active sites if it is non-selective. Olsbye et al. elucidated the effect of deactivation on MTH product selectivity in a series of contributions where catalysts were tested at different contact times. They found that deactivation is non-selective over H-ZSM-5¹⁴⁶, ZSM-11, IM-5, TNU-9¹¹², ZSM-22, ZSM-23, EU-1¹⁴⁸ and SAPO-5¹⁴⁹. Over these catalysts, deactivation seems to occur simply as a loss of active sites. The one prominent exception from the series of studies was H-SAPO-34,

which shows an increase in the ethene-to-propene ratio with time on stream.^{7,8,102,120}

Two more requirements need to be fulfilled to employ Janssens' model in catalyst comparisons: First, the initiation zone of the catalyst bed must be negligible, since the model does not take into account a critical contact time (Fig. 21-22), and second, methanol must be a main source of hydrocarbon deposits in both catalyst, as indicated by the conversion versus time on stream behavior (Fig. 20). Both prerequisites were found to be fulfilled for H-ZSM-5¹⁴⁶. However, for H-ZSM-22, which also led to an S-shaped deactivation curve, the methanol conversion capacity was found to increase steadily with increasing contact time, thus suggesting a non-negligible initiation zone.¹¹⁰ To allow for a wider applicability of quantitative stability comparisons, the two groups joined forces to develop the Autocatalytic deactivation model, in which an initiation zone is accounted for.¹¹¹ In the Autocatalytic deactivation model, product formation is set to proceed by reactions (2.10) and (2.11) in parallel. The loss of active sites with time on stream is set to be first order in methanol partial pressure, and proportional to methanol conversion, as it was in Janssens' model. Testing of two different catalysts, H-ZSM-5 and H-ZSM-22, at several contact times yielded a linear plot of the time on stream needed to reach 50 % conversion versus contact time for each catalyst (Fig. 25). The methanol conversion capacity was much higher for H-ZSM-5 than for H-ZSM-22. Furthermore, as indicated by Fig. 25, the initiation zone (critical contact time) was significant for H-ZSM-22, while it was negligible for H-ZSM-5. Furthermore, the reaction rate observed over H-ZSM-22 was much lower than for H-ZSM-5, even if H-ZSM-22 was tested at 50 °C higher temperature.¹¹¹

(Fig. 25)

The examples above show the usefulness of such quantitative models. In an on-going study, the concept of the Autocatalytic deactivation model is applied to a larger number of zeolite topologies. So far, the applicability of the model has been confirmed for topologies with similar or smaller pore size than H-ZSM-5 (H-ZSM-22, H-ZSM-23, IM-5, TNU-9).¹⁵⁰

Janssens' model and the Autocatalytic model both assume full initial conversion, and do not take into account the formation of active species with time on stream. This simplification is justified in studies performed at full initial conversion, where steady-state product selectivities are observed after a few minutes on stream. The models however fall short of describing studies performed at less than 100 % initial conversion, where a slower formation and accumulation of active species is observed, see e.g. H-SAPO-34 in ¹⁰⁷ and H-ZSM-5 in ¹⁴⁶. Such formation and deactivation was fully accounted for in two recent hydrocarbon pool models, published in Wragg et al¹⁵¹ (see below) and Janssens et al¹¹¹, respectively. However, these models contain too many unknown parameters to enable quantification of deactivation kinetics based on ordinary catalytic tests, and currently require operando measurements to simultaneously monitor formation and degradation of active species.

2.4.3 Time- and space-resolved reactor studies. A break-through in the understanding of the time-on-stream behavior of H-SAPO-34 as MTH catalyst was achieved when Wragg and coworkers employed

time- and space-resolved X-Ray Diffraction (XRD) to monitor the formation of hydrocarbon species in the catalyst during operation in a laboratory scale microreactor (Fig. 26).¹⁵¹ The study built on several previous contributions, where the group had observed a correlation between the CHA unit cell parameters (in particular an expansion along the crystallographic *c* axis) and the formation of hydrocarbon species, by a combination of crystallographic and computational studies.¹⁵²⁻¹⁵⁴ In the operando time- and space-resolved study, it was observed that *c*-axis expansion, observed as a color change from dark blue to light blue/green in Fig. 26, occurred 2-3 mm into the bed, and expanded forward and backward before filling the entire bed after ~ 8 min on stream. Simultaneously, the methanol conversion to alkenes, observed by the lines in Fig. 26, increased. With longer times on stream a further expansion (yellow—red color), which was interpreted as formation of heavy polyaromatic coke species, started 1–2 mm into the catalyst bed, and expanded towards the end of the bed with TOS. This evolution was accompanied by a simultaneous decrease in methanol conversion.¹⁵¹

(Fig. 26)

A kinetic model, which described the formation of arene intermediates and its gradual transformation to coke precursors in each catalyst segment with time on stream was developed, and successfully simulated the observations made by XRD (Fig. 27). Note that the color coding of Fig. 26 and 27, respectively, are not the same.

(Fig. 27)

Bleken et al recently published a study of parent and desilicated H-ZSM-5, in which the catalyst was partially deactivated during MTH at elevated reaction pressure, before the catalyst beds were fractionated from top to bottom of the reactor bed.¹⁵⁵ Thorough analysis of the fractions showed that the parent material was most deactivated near the entrance of the catalyst bed, whereas the desilicated sample was more deactivated towards the end of the catalyst bed. A complex interplay of alterations of porosity, activity, and rate of deactivation was suggested as an explanation to the more uniform deactivation of the desilicated catalyst.

The initiation zone has so far been scarcely considered in deactivation studies. However, two recent contributions from Lercher et al. offer a novel approach to the subject. In the first study, it was observed that the methanol conversion capacity of a H-ZSM-5 catalyst increased remarkably when co-feeding light alkenes to the reactor at 475 °C.¹⁵⁶ The authors suggested that methanol is a source of coke formation via rather slow, initial redox reactions which eventually lead to coke formation, evidenced by a high initial selectivity to methane. In the presence of alkenes, they suggested that the faster methylation reactions would out-compete the redox reactions.¹⁵⁶ In a very recent contribution, Lercher et al. presented a comparative study of H-ZSM-5 catalyst deactivation during testing in a PFR and a CSTR reactor, respectively, at 450 °C, with WHSV in the range 0.5 – 22 h g/mol.¹⁰¹ The methanol conversion varied between 0 and 100 % in the PFR reactor, with a clear indication of an initiation zone (i.e.; close to zero conversion at contact times below 2 h g/mol). In the CSTR reactor, conversions ranging from 0 to around 90 % were observed, without an initiation

zone. Due to the excellent mixing conditions, each test in the CSTR reactor might therefore be considered as representing a thin segment of the autocatalytic zone in a PFR reactor (Fig. 22). Significantly different deactivation rates were observed between the two reactors. The authors ascribed the different deactivation behavior to the different local methanol concentration in the two reactors, leading to less formation of poisoning species in the CSTR reactor. A reaction mechanism for the formation of aromatic hydrocarbon deposits via oxygenates formed from methanol in the initiation zone was suggested. This mechanism was proposed as the main source of catalyst deactivation in the plug flow reactor.¹⁰¹

Conclusions

Since the discovery of MTH process in 1970s, many efforts have been devoted to fundamental understanding of the initial C-C bond formation mechanism. Although both operando and theoretical studies supported the occurrence of a direct mechanism and definitely show the formation of surface methoxy species (SMS) before the generation of hydrocarbon species, there is only one of the proposed direct routes that can reasonably account for the formation of the first C-C bond; the recently suggested methoxymethylation ($\text{CH}_3\text{OCH}_2^+$) mechanism which not only yielded new insight into the first C-C bond formation, but also rationalized the build-up of the HCP species.

Four decades of MTH studies have led to rather detailed insight in the formation of deactivating hydrocarbon species, especially for the two commercial catalysts, H-ZSM-5 and H-SAPO-34. Recently, mathematical tools were developed which allow for representative catalyst stability comparisons relating to the autocatalytic zone of a plug flow reactor. A protocol where tests are performed at several contact times, all giving 100 % initial conversion, has been proposed to eliminate the influence of the initiation zone. Recent studies however suggest that the initiation zone may deserve further attention as a source of coke formation.

Recent developments within operando catalyst studies have provided novel insight in coke formation at the micro-, meso- and macro-scale. Operando measurements in combination with kinetic models based on mechanistic insight represent a powerful tool for further catalyst optimisation.

Acknowledgements

U.O., S.S. and K.P.L. acknowledge the Norwegian Research Council for financial support under contract no. 174893. Z. W., Y. C., J. L., J. W. and W. F. acknowledge the National Basic Research Program (2011CB201403 and 2011CB201406), the National Natural Science Foundation of China (21103216, 21273263 and 21273264) and the Natural Science Foundation of Shanxi Province of China (2013021007-3 and 2015021003) for financial support.

References

- 1 Chang, C. D.; Silvestri, A. J. *J. Catal.*, 1977, **47**, 249-259.

- 2 S. Teketel, M. Westgård Erichsen, F.L. Bleken, S. Svelle, K.P. Lillerud, U. Olsbye in J. Spivey, Y.-F. Han, K. Dooley (Ed.s) *Catalysis: Volume 26*, Royal Society of Chemistry (2014) 179-217.
- 3 C. D. Chang, *Catal. Rev. Sci. Eng.* 1983, **25**, 1-118.
- 4 M. Stöcker, *Microporous Mesoporous Mater.*, 1999, **29**, 3-48.
- 5 F. J. Keil, *Microporous Mesoporous Mater.*, 1999, **29**, 49-66.
- 6 C. D. Chang in *Shape Selective Catalysis: Chemical Synthesis and Hydrocarbon Processing* (Eds.: C. Song, J. M. Garcés, Y. Sugi), ACS, Washington, 2000, p. 96 (ACS Symp. Ser. 738).
- 7 W. Song, H. Fu and J. F. Haw, *J. Am. Chem. Soc.*, 2001, **123**, 4749-4754.
- 8 P. Barger in *Zeolites for Cleaner Technologies*, (Eds.: M. Guisnet, J.-P. Wilson), Imperial College Press, London, 2002, p. 239 (Catal. Sci. Ser. Vol. 3).
- 9 J. F. Haw, D. M. Marcus in *Handbook of Zeolite Science and Technology* (Eds: S. M. Auerbach, K. A. Carrado, P. K. Dutta), Marcel Dekker, New York, 2003, p. 833.
- 10 S. Kvisle, T. Fuglerud, S. Kolboe, U. Olsbye, K.P. Lillerud, B.P. Vora in H. Ertl, F. Knözinger, F. Schüth and J. Weitkamp (Ed.s), *Handbook of Heterogeneous Catalysis* (2nd Edition) Wiley-VCH 6 (2008) 2950-2965.
- 11 S. Svelle, M. Visur, U. Olsbye, Saepurahman, M. Bjorgen, *Top. Catal.*, 2011, **54**, 897-906.
- 12 U. Olsbye, S. Svelle, M. Bjørgen, P. Beato, T.V.W. Janssens, F. Joensen, S. Bordiga, K.P. Lillerud, *Angew. Chem., Int. Ed.*, 2012, **51**, 5810-5831.
- 13 S. Ilias and A. Bhan, *ACS Catal.*, 2013, **3**, 18-31.
- 14 K. Hemelsoet, J. Van der Mynsbrugge, K. De Wispelaere, M. Waroquier, V. Van Speybroeck, *ChemPhysChem*, 2013, **14**, 1526-1545.
- 15 M.W. Erichsen, J. S. Martinez-Espin, F. Joensen, S. Teketel, P.D.C. Huertas, K.P. Lillerud, S. Svelle, P. Beato, U. Olsbye in: N. Kanellopoulos (Ed.) *Small-Scale Gas to Liquid Fuel Synthesis*. CRC Press (2015) 441-473.
- 16 S. Svelle, F. Joensen, J. Nerlov, U. Olsbye, K. P. Lillerud, S. Kolboe, M. Bjørgen, *J. Am. Chem. Soc.*, 2006, **128**, 14770-14771.
- 17 M. Bjørgen, S. Svelle, F. Joensen, J. Nerlov, S. Kolboe, F. Bonino, L. Palumbo, S. Bordiga, U. Olsbye, *J. Catal.*, 2007, **248**, 195-207.
- 18 M. Westgård Erichsen, S. Svelle and U. Olsbye, *Catal. Today*, 2013, **215**, 216-223.
- 19 D. Lesthaeghe, V. Van Speybroeck, G. B. Marin and M. Waroquier, *Angew. Chem. Int. Ed.*, 2006, **45**, 1714-1719.
- 20 D. Lesthaeghe, V. Van Speybroeck, G. B. Marin and M. Waroquier, *Ind. Eng. Chem. Res.*, 2007, **46**, 8832-8838.
- 21 D. Lesthaeghe, V. Van Speybroeck, G. B. Marin and M. Waroquier, *Chem. Phys. Lett.*, 2006, **417**, 309-315.
- 22 I. M. Dahl and S. Kolboe, *Catal. Lett.*, 1993, **20**, 329-336.
- 23 W. Song, J. F. Haw, J. B. Nicholas and C. S. Heneghan, *J. Am. Chem. Soc.*, 2000, **122**, 10726-10727.
- 24 I. M. Dahl and S. Kolboe, *J. Catal.*, 1994, **149**, 458-464.
- 25 W. Dai, C. Wang, M. Dyballa, G. Wu, N. Guan, L. Li, Z. Xie and M. Hunger, *ACS Catal.*, 2014, 317-326.
- 26 Y. Jiang, W. Wang, V. Reddy Marthala, J. Huang, B. Sulikowski and M. Hunger, *J. Catal.*, 2006, **238**, 21-27.
- 27 T. Xu and J. F. Haw, *J. Am. Chem. Soc.*, 1994, **116**, 7753-7759.
- 28 P. W. Goguen, T. Xu, D. H. Barich, T. W. Skloss, W. Song, Z. Wang, J. B. Nicholas and J. F. Haw, *J. Am. Chem. Soc.*, 1998, **120**, 2650-2651.
- 29 J. F. Haw, J. B. Nicholas, W. Song, F. Deng, Z. Wang, T. Xu and C. S. Heneghan, *J. Am. Chem. Soc.*, 2000, **122**, 4763-4775.
- 30 D. M. McCann, D. Lesthaeghe, P. W. Kletnieks, D. R. Guenther, M. J. Hayman, V. Van Speybroeck, M. Waroquier and J. F. Haw, *Angew. Chem. Int. Ed.*, 2008, **47**, 5179-5182.
- 31 S. Xu, A. Zheng, Y. Wei, J. Chen, J. Li, Y. Chu, M. Zhang, Q. Wang, Y. Zhou and J. Wang, *Angew. Chem. Int. Ed.*, 2013, **125**, 11564-11568.
- 32 C. Wang, Y. Chu, A. Zheng, J. Xu, Q. Wang, P. Gao, G. Qi, Y. Gong and F. Deng, *Chem. Eur. J.*, 2014, **20**, 12432-12443.
- 33 J. F. Haw, B. R. Richardson, I. S. Oshiro, N. D. Lazo and J. A. Speed, *J. Am. Chem. Soc.*, 1989, **111**, 2052-2058.
- 34 W. Song, J. B. Nicholas and J. F. Haw, *J. Phys. Chem. B*, 2001, **105**, 4317-4323.
- 35 T. Xu, D. H. Barich, P. W. Goguen, W. Song, Z. Wang, J. B. Nicholas and J. F. Haw, *J. Am. Chem. Soc.*, 1998, **120**, 4025-4026.
- 36 A. Sassi, M. A. Wildman, H. J. Ahn, P. Prasad, J. B. Nicholas and J. F. Haw, *J. Phys. Chem. B*, 2002, **106**, 2294-2303.
- 37 W. Song, J. B. Nicholas, A. Sassi and J. F. Haw, *Catal. Lett.*, 2002, **81**, 49-53.
- 38 J. Li, Y. Wei, J. Chen, P. Tian, X. Su, S. Xu, Y. Qi, Q. Wang, Y. Zhou and Y. He, *J. Am. Chem. Soc.*, 2012, **134**, 836-839.
- 39 Q. Qian, C. Vogt, M. Mokhtar, A. M. Asiri, S. A. Al-Thabaiti, S. N. Basahel, J. Ruiz-Martínez and B. M. Weckhuysen, *ChemCatChem*, 2014, **6**, 3396-3408.
- 40 J. B. Nicholas and J. F. Haw, *J. Am. Chem. Soc.*, 1998, **120**, 11804-11805.
- 41 J. B. Nicholas, T. Xu and J. F. Haw, *Top. Catal.*, 1998, **6**, 141-149.
- 42 J. F. Haw, W. Song, D. M. Marcus and J. B. Nicholas, *Acc. Chem. Res.*, 2003, **36**, 317-326.
- 43 J. Li, Y. Wei, Y. Qi, P. Tian, B. Li, Y. He, F. Chang, X. Sun and Z. Liu, *Catal. Today*, 2011, **164**, 288-292.
- 44 Y. Ono and T. Mori, *J. Chem. Soc., Faraday Trans. 1*, 1981, **77**, 2209-2221.
- 45 Y. Jiang, W. Wang, V. R. Reddy Marthala, J. Huang, B. Sulikowski and M. Hunger, *J. Catal.*, 2006, **244**, 134-136.
- 46 W. Wang, A. Buchholz, M. Seiler and M. Hunger, *J. Am. Chem. Soc.*, 2003, **125**, 15260-15267.
- 47 W. Song, D. M. Marcus, H. Fu, J. O. Ehresmann and J. F. Haw, *J. Am. Chem. Soc.*, 2002, **124**, 3844-3845.
- 48 Z. Cui, Q. Liu, S. Bain, Z. Ma and W. Song, *J. Phys. Chem. C*, 2008, **112**, 2685-2688.
- 49 D. M. Marcus, K. A. McLachlan, M. A. Wildman, J. O. Ehresmann, P. W. Kletnieks and J. F. Haw, *Angew. Chem. Int. Ed.*, 2006, **45**, 3133-3136.
- 50 J. F. Haw, D. M. Marcus and P. W. Kletnieks, *J. Catal.*, 2006, **244**, 130-133.
- 51 H. Yamazaki, H. Shima, H. Imai, T. Yokoi, T. Tatsumi and J. N. Kondo, *J. Phys. Chem. C*, 2012, **116**, 24091-24097.
- 52 H. Yamazaki, H. Shima, H. Imai, T. Yokoi, T. Tatsumi and J. N. Kondo, *Angew. Chem. Int. Ed.*, 2011, **50**, 1853-1856.
- 53 J. Li, Z. Wei, Y. Chen, B. Jing, Y. He, M. Dong, H. Jiao, X. Li, Z. Qin, J. Wang and W. Fan, *J. Catal.*, 2014, **317**, 277-283.
- 54 T. Forester and R. Howe, *J. Am. Chem. Soc.*, 1987, **109**, 5076-5082.
- 55 E. J. Munson, N. D. Lazo, M. E. Moellenhoff and J. F. Haw, *J. Am. Chem. Soc.*, 1991, **113**, 2783-2784.
- 56 M. W. Anderson and J. Klinowski, *J. Am. Chem. Soc.*, 1990, **112**, 10-16.
- 57 E. P. Grimsrud and P. Kebarle, *J. Am. Chem. Soc.*, 1973, **95**, 7939-7943.
- 58 S. D. Hellring, K. D. Schmitt and C. D. Chang, *J. Chem. Soc., Chem. Commun.*, 1987, 1320-1322.
- 59 E. J. Munson and J. F. Haw, *J. Am. Chem. Soc.*, 1991, **113**, 6303-6305.
- 60 J. van den Berg, J. Wolthuizen and J. van Hooff, in *Proceedings 5th International Zeolite Conference*, Heyden, London, Naples, Italy, 1980.
- 61 G. A. Olah, H. Doggweiler, J. D. Felberg, S. Frohlich, M. J. Grdina, R. Karpeles, T. Keumi, S. Inaba, W. M. Ip and K. Lammertsma, *J. Am. Chem. Soc.*, 1984, **106**, 2143-2149.
- 62 E. J. Munson, A. A. Kheir, N. D. Lazo and J. F. Haw, *J. Phys. Chem.*, 1992, **96**, 7740-7746.
- 63 D. N. Kevill and G. M. L. Lin, *J. Am. Chem. Soc.*, 1979, **101**, 3916-3919.

- 64 E. A. Swabb and B. C. Gates, *Ind. Eng. Chem. Fundam.*, 1972, **11**, 540-545.
- 65 P. Salvador and W. Kladnig, *J. Chem. Soc., Faraday Trans. 1*, 1977, **73**, 1153-1168.
- 66 W. Wang, M. Seiler and M. Hunger, *J. Phys. Chem. B*, 2001, **105**, 12553-12558.
- 67 W. Wang and M. Hunger, *Acc. Chem. Res.*, 2008, **41**, 895-904.
- 68 P. E. Sinclair and C. R. A. Catlow, *J. Phys. Chem. B*, 1997, **101**, 295-298.
- 69 L. Kubelková, J. Nováková and P. Jírů, *Stud. Surf. Sci. Catal.*, 1984, **18**, 217-224.
- 70 J. Nováková, L. Kubelková and Z. Dolejšek, *J. Catal.*, 1986, **97**, 277-279.
- 71 J. Nováková, L. Kubelková and Z. Dolejšek, *J. Catal.*, 1987, **108**, 208-213.
- 72 G. J. Hutchings, F. Gottschalk, M. M. Hall and R. Hunter, *J. Chem. Soc., Faraday Trans. 1*, 1987, **83**, 571-583.
- 73 G. J. Hutchings, F. Gottschalk and R. Hunter, *Ind. Eng. Chem. Res.*, 1987, **26**, 635-637.
- 74 L. Kubelková, J. Nováková and K. Nedomová, *J. Catal.*, 1990, **124**, 441-450.
- 75 S. R. Blaszowski and R. A. van Santen, *J. Am. Chem. Soc.*, 1997, **119**, 5020-5027.
- 76 N. Tajima, T. Tsuneda, F. Toyama and K. Hirao, *J. Am. Chem. Soc.*, 1998, **120**, 8222-8229.
- 77 T. R. Forester, S.-T. Wong and R. F. Howe, *J. Chem. Soc., Chem. Commun.*, 1986, 1611-1613.
- 78 J. Rakoczy and T. Romotowski, *Zeolites*, 1993, **13**, 256-260.
- 79 G. Mirth and J. A. Lercher, *J. Phys. Chem.*, 1991, **95**, 3736-3740.
- 80 P. Cheung, A. Bhan, G. J. Sunley, D. J. Law and E. Iglesia, *J. Catal.*, 2007, **245**, 110-123.
- 81 F. Salehirad and M. W. Anderson, *J. Catal.*, 1996, **164**, 301-314.
- 82 I. I. Ivanova, E. B. Pomakhina, A. I. Rebrov, M. Hunger, Y. G. Kolyagin and J. Weitkamp, *J. Catal.*, 2001, **203**, 375-381.
- 83 I. M. Hill, Y. S. Ng and A. Bhan, *ACS Catal.*, 2012, **2**, 1742-1748.
- 84 I. M. Hill, A. Malek and A. Bhan, *ACS Catal.*, 2013, **3**, 1992-2001.
- 85 P. Cheung, A. Bhan, G. J. Sunley and E. Iglesia, *Angew. Chem. Int. Ed.*, 2006, **45**, 1617-1620.
- 86 A. Bhan, A. D. Allian, G. J. Sunley, D. J. Law and E. Iglesia, *J. Am. Chem. Soc.*, 2007, **129**, 4919-4924.
- 87 A. Bhan and E. Iglesia, *Acc. Chem. Res.*, 2008, **41**, 559-567.
- 88 J. Van der Mynsbrugge, S. L. C. Moors, K. De Wispelaere and V. Van Speybroeck, *ChemCatChem*, 2014, **6**, 1906-1918.
- 89 T. Maihom, B. Boekfa, J. Sirirajraensre, T. Nanok, M. Probst and J. Limtrakul, *J. Phys. Chem. C*, 2009, **113**, 6654-6662.
- 90 R. Martin, F. Lampe and R. Taft, *J. Am. Chem. Soc.*, 1966, **88**, 1353-1357.
- 91 F. E. Celik, T. Kim, A. N. Mlinar and A. T. Bell, *J. Catal.*, 2010, **274**, 150-162.
- 92 E. D. Glendening, J. K. Badenhop, A. E. Reed, J. E. Carpenter, J. A. Bohmann, C. M. Morales, C. R. Landis and F. Weinhold, *NBO 6.0*, <http://nbo6.chem.wisc.edu/>.
- 93 G. A. Olah and J. M. Bollinger, *J. Am. Chem. Soc.*, 1967, **89**, 2993-2996.
- 94 Z. Wei, Y. Chen, J. Li, B. Jing, Y. He, M. Dong, H. Jiao, Z. Qin, J. Wang and W. Fan, submitted to *Journal of Catalysis*, 2015.
- 95 NIST Standard Reference Database 85, NIST/TRC Table Database, WinTable, Version 2003.
- 96 A.G. Gayubo, P.L. Benito, A.T. Aguayo, M. Castilla, J. Bilbao, *Chem. Eng. Sci.*, 1996, **51**, 3001-3006.
- 97 P. Magnoux, P. Roger, C. Canaff, V. Fouche, N.S. Gnep, M. Guisnet, *Stud. Surf. Sci. Catal.*, 1987, **34**, 317-330.
- 98 D. Mores, E. Stavitski, M.H.F. Kox, J. Kornatowski, U. Olsbye, B.M. Weckhuysen, *Chem. Eur. J.*, 2008, **14**, 11320-11327.
- 99 L. Palumbo, F. Bonino, P. Beato, M. Bjørgen, A. Zecchina, S. Bordiga, *J. Phys. Chem. C*, 2008, **112**, 9710-9716.
- 100 P. Beato, E. Schachtl, K. Barbera, F. Bonino, S. Bordiga, *Cat. Today*, 2013, **205**, 128-133.
- 101 S. Müller, Y. Liu, M. Vishnuvarthan, X. Sun, A.C. van Veen, G.L. Haller, M. Sanchez-Sanchez, J.A. Lercher, *J. Catal.*, 2015, **325**, 48-59.
- 102 D. Chen, K. Moljord, T. Fuglerud, A. Holmen, *Microporous Mesoporous Mater.*, 1999, **29**, 191-203.
- 103 J.P. Hofmann, D. Mores, L.R. Aramburo, S. Teketel, M. Rohnke, J. Janek, U. Olsbye, B.M. Weckhuysen, *Chem. Eur. J.*, 2013, **19**, 8533-8542.
- 104 S. Teketel, U. Olsbye, K.P. Lillerud, P. Beato, S. Svelle, *Microporous Mesoporous Mater.*, 2010, **136**, 33-41.
- 105 M. Bjørgen, F. Joensen, K.P. Lillerud, U. Olsbye, S. Svelle, *Cat. Today*, 2009, **142**, 90-97.
- 106 B. Arstad, S. Kolboe, *J. Am. Chem. Soc.*, 2001, **123**, 8137-8138.
- 107 B. P. C. Hereijgers, F. Bleken, M. H. Nilsen, S. Svelle, K. P. Lillerud, M. Bjørgen, B. M. Weckhuysen, U. Olsbye, *J. Catal.*, 2009, **264**, 77-87.
- 108 W. Song, H. Fu, J. F. Haw, *J. Phys. Chem. B*, 2001, **105**, 12839-12843.
- 109 M. Bjørgen, U. Olsbye, D. Petersen, S. Kolboe, *J. Catal.*, 2004, **221**, 1-10.
- 110 S. Teketel, S. Svelle, K.P. Lillerud, U. Olsbye, *ChemCatChem*, 2009, **1**, 78-81.
- 111 T.V.W. Janssens, S. Svelle, U. Olsbye, *J. Catal.*, 2013, **308**, 122-130.
- 112 F. Bleken, W. Skistad, K. Barbera, M. Kustova, S. Bordiga, P. Beato, K. P. Lillerud, S. Svelle, U. Olsbye, *Phys. Chem. Chem. Phys.*, 2011, **13**, 2539-2549.
- 113 J. W. Park, J. Y. Lee, K. S. Kim, S. B. Hong, G. Seo, *Appl. Catal. A*, 2008, **339**, 36-44.
- 114 L.-T. Yuen, S. I. Zones, T. V. Harris, E. J. Gallegos, A. Auroux, *Microporous Mater.*, 1994, **2**, 105-117.
- 115 S. Wilson, P. Barger, *Microporous Mesoporous Mater.*, 1999, **29**, 117-126.
- 116 Q. Zhu, J. N. Kondo, R. Ohnuma, Y. Kubota, M. Yamaguchi, T. Tatsumi, *Microporous Mesoporous Mater.*, 2008, **112**, 153-161.
- 117 I. M. Dahl, H. Mostad, D. Akporiaye, R. Wendelbo, *Microporous Mesoporous Mater.*, 1999, **29**, 185-190.
- 118 D. Mores, J. Kornatowski, U. Olsbye, B. M. Weckhuysen, *Chem. Eur. J.*, 2011, **17**, 2874-2884.
- 119 D. Chen, K. Moljord, T. Fuglerud, A. Holmen, *Microporous Mesoporous Mater.*, 1999, **29**, 191-203.
- 120 I. M. Dahl, R. Wendelbo, A. Andersen, D. Akporiaye, H. Mostad, T. Fuglerud, *Microporous Mesoporous Mater.*, 1999, **29**, 159-171.
- 121 M. Bjørgen, U. Olsbye, S. Kolboe, *J. Catal.*, 2003, **215**, 30-44.
- 122 M. Bjørgen, S. Akyalcin, U. Olsbye, S. Benard, S. Kolboe, S. Svelle, *J. Catal.*, 2010, **275**, 170-180.
- 123 H. Schulz, *Catal. Today*, 2010, **154**, 183-194.
- 124 M. Bjørgen, F. Joensen, M. Spangsborg Holm, U. Olsbye, K.-P. Lillerud, S. Svelle, *Appl. Catal. A*, 2008, **345**, 43-50.
- 125 J. Kim, M. Choi, R. Ryoo, *J. Catal.*, 2010, **269**, 219-228.
- 126 S. Fathi, M. Sohrabi, C. Falamaki, *Fuel*, 2014, **116**, 529-537.
- 127 S. Svelle, L. Sommer, K. Barbera, P.N.R. Vennestrøm, U. Olsbye, K.P. Lillerud, S. Bordiga, Y.-H. Pan, P. Beato, *Catal. Today*, 2011, **168**, 38-47.
- 128 Y. Ni, A. Sun, X. Wu, G. Hai, J. Hu, T. Li, G. Li, *J. Natural Gas Chem.*, 2011, **20**, 237-242.
- 129 P. Sazama, B. Wichterlova, J. Dedecek, Z. Tvaruzkova, Z. Musilova, L. Palumbo, S. Sklenak, O. Gonsiorova, *Microporous Mesoporous Mater.*, 2011, **143**, 87-96.

ARTICLE

Journal Name

- 130 F. Lønstad Bleken, K. Barbera, F. Bonino, U. Olsbye, K.P. Lillerud, S. Bordiga, P. Beato, T.V.W. Janssens, S. Svelle, *J. Catal.*, 2013, **307**, 62-73.
- 131 C. Mei, P. Wen, Z. Liu, H. Liu, Y. Wang, W. Yang, Z. Xie, W. Hua, Z. Gao, *J. Catal.*, 2008, **258**, 243-249.
- 132 M. Choi, K. Na, J. Kim, Y. Sakamoto, O. Terasaki, R. Ryoo, *Nature*, 2009, **461**, 246-250.
- 133 B. Arstad, S. Kolboe, *Catal. Lett.*, 2001, **71**, 209-212.
- 134 H. Fu, W. Song, J.F. Haw, *Catal. Lett.*, 2001, **76**, 89-94.
- 135 W. Song, H. Fu, J.F. Haw, *J. Phys. Chem. B*, 2001, **105**, 12839-12843.
- 136 F. Bleken, M. Bjorgen, L. Palumbo, S. Bordiga, S. Svelle, K. P. Lillerud, U. Olsbye, *Top. Catal.*, 2009, **52**, 218-228.
- 137 T.V.W. Janssens, *J. Catal.*, 2009, **264**, 130-137.
- 138 C.D. Chang, *Catal. Rev. – Sci. Eng.*, 1984, **26**, 323-345.
- 139 C.-M. Wang, Y.-D. Wang, Z.-K. Xie, Z.-P. Liu, *J. Phys. Chem. C*, 2009, **113**, 4584-4591.
- 140 D. Lesthaeghe, A. Horre, M. Waroquier, G. B. Marin, V. Van Speybroeck, *Chem. Eur. J.*, 2009, **15**, 10803-10808.
- 141 B. Chan, L. Radom, *Can. J. Chem.* 2010, **88**, 866-876.
- 142 C.-M. Wang, Y.-D. Wang, H.-X. Liu, Z.-K. Xie, Z.-P. Liu, *J. Catal.*, 2010, **271**, 386-391.
- 143 M. Bjorgen, S. Akyalcin, U. Olsbye, S. Benard, S. Kolboe, S. Svelle, *J. Catal.*, 2010, **275**, 170-180.
- 144 J. F. Haw, D. M. Marcus, *Top. Catal.*, 2005, **34**, 41-48.
- 145 M. Kaarsholm, F. Joensen, J. Nerlov, R. Cenni, J. Chaouki, G. S. Patience, *Chem. Eng. Sci.*, 2007, **62**, 5527-5532.
- 146 F.L. Bleken, T.V.W. Janssens, S. Svelle, U. Olsbye *Micropor. Mesopor. Mater.*, 2012, **164**, 190-198.
- 147 K. Barbera, F. Bonino, S. Bordiga, T.V.W. Janssens, P. Beato, *P. J. Catal.*, 2011, **280**, 196-205.
- 148 S. Teketel, W. Skistad, S. Benard, U. Olsbye, K.P. Lillerud, P. Beato, S. Svelle, *ACS Catal.*, 2012, **2**, 26-37.
- 149 M. Westgaard Erichsen, S. Svelle, U. Olsbye, *J. Catal.*, 2013, **298**, 94-101.
- 150 S. Etemadi, M.Sc. Thesis, University of Oslo, 2015.
- 151 D. Wragg, M.G. O'Brien, F.L. Bleken, M. Di Michiel, U. Olsbye, H. Fjellvåg, *Angew. Chemie Int. Ed.*, 2012, **51**, 7956-7959.
- 152 D. S. Wragg, R. E. Johnsen, M. Balasundaram, P. Norby, H. Fjellvåg, A. Grønvold, T. Fuglerud, J. Hafizovic, Ø. B. Vistad, D. Akporiaye, *J. Catal.*, 2009, **268**, 290 – 296.
- 153 D. S. Wragg, R. E. Johnsen, P. Norby, H. Fjellvåg, *Microporous Mesoporous Mater.*, 2010, **134**, 210 – 215.
- 154 M. Zokaie, D. S. Wragg, A. Grønvold, T. Fuglerud, J.H. Cavka, K. P. Lillerud, O. Swang, *Microporous Mesoporous Mater.*, 2013, **165**, 1-5.
- 155 F.L. Bleken, K. Barbera, F. Bonino, U. Olsbye, K.P. Lillerud, S. Bordiga, P. Beato, T.V.W. Janssens, S. Svelle *J. Catal.*, 2013, **307**, 62-73.
- 156 X.Y. Sun, S. Mueller, Y. Liu, H. Shi, G.L. Haller, : Sanchez-Sanchez, A.C. Van Veen, J.A. Lercher *J. Catal.*, 2014, **317**, 185-197.

Figure captions

Fig. 1 The “dual-cycle” mechanism. Reproduced from ¹⁸.

Fig. 2 Schematic illustration of oxonium ylide mechanism.

Fig. 3 Schematic routes of carbene mechanism (a) α -elimination of water from methanol; (b) decomposition of SMS.

Fig. 4 Schematic illustration of methane-formaldehyde mechanism.

Fig. 5 Experimental evidence for the direct mechanism. (a) Methanol (blue square) and DME (brown solid circle) conversions obtained at different pulses in the MTO process catalyzed by FC-SAPO-34 and the DME conversions (brown hollow circle) attained after successively injecting various times of methanol, e.g. the DME conversions at the pulse of 3, 4, 5 and 6 refer to the values obtained by pulsing DME after successive injection of 2, 3, 4 and 5 times of methanol. Experimental methods: 100 mg of FC-SAPO-34 was first pretreated at 550 °C for 2 h in air before the reaction, which was carried out at 400 °C with Ar as carrier gas, the flow rate of which is 300 mL/min. Every time 0.07 mmol of methanol or 0.035 mmol of DME was injected. The methanol and DME conversions were calculated by considering both of them in the effluents as unreacted substrates. (b) Reaction results of ¹³C-methanol over the NFC-SAPO-34, which was activated at 550 °C in Ar atmosphere before pulsing 0.005 mmol of ¹³C-methanol. Reproduced from ⁵³.

Fig. 6 IR spectra for the formation of methoxy groups from methanol and DME. (a) 200 Pa of methanol was introduced into the IR cell equipped with 30 mg of FC-SAPO-34 self-supported wafer at 50 °C. The spectra were recorded from 50 to 300 °C with the temperature ramp rate of 5 °C/min. (b) 200 Pa of DME was introduced as reactant and spectra were obtained according to the same procedures as those employed in Fig. 6(a). (c) DME reacted at 300 °C for 30 s at different pressures.

Fig. 7 (a) Unassisted and (b) assisted methoxide formation. Reproduced from ⁸⁸.

Fig. 8 DFT calculation results for the formation of methoxy group from methanol or DME (The blue numbers represent the energy barriers (kJ/mol), while the orange and green numbers in parentheses are their rate constants (s^{-1}) at 250 and 400 °C respectively). Reproduced from ⁵³.

Fig. 9 Transition states for a,b) unassisted and c,d) methanol-assisted methoxide formation from a,c) methanol and b,d) dimethyl ether. Reproduced from ⁸⁸.

Fig. 10 Schematic illustration of the methoxymethyl mechanism.

Fig. 11 Route for the formation of the first C–C bond from surface methoxy and DME. The blue numbers represent the energy barriers (kJ/mol), while the orange and green numbers in parentheses are

the rate constants (s^{-1}) at 250 and 400 °C respectively. Reproduced from ⁵³.

Fig. 12 The structures of initial states, transition states and final states of the two steps in the methoxymethyl mechanism.

Fig. 13 IR spectra for the formation of $CH_3OCH_2^+$ by the reaction of methoxy group and DME. Experimental methods: 6.5 Pa of DME was introduced into the IR cell equipped with 30 mg of CH_3O -formed FC-SAPO-34 self-supported wafer at 30 °C. The spectra were recorded from 30 to 180 °C with a temperature ramp rate of 5 °C/min. The spectra recorded at 30 and 180 °C were denoted as $CH_3O+DME(30^\circ C)$ and $CH_3O+DME(180^\circ C)$ respectively. The spectra of $DMM(30^\circ C)$ and $DMM(180^\circ C)$ were obtained by introducing 6.5 Pa of dimethoxymethane into the IR cell equipped with 30 mg of the pretreated FC-SAPO-34 self-supported wafer at 30 °C, and then increasing the temperature to 180 °C. The spectra of $DME(30^\circ C)$ and $DME(180^\circ C)$ were obtained according to the same procedures as those employed for measuring $DMM(30^\circ C)$ and $DMM(180^\circ C)$ except that DME was introduced. Reproduced from ⁵³.

Fig. 14 NRT analysis of $(CH_2OCH_3)^+$ ion at MP2/cc-pVQZ level.

Fig. 15 Gibbs energy of formation per C atom (kJ/mol) for reactant and product molecules associated with the MTH process in the temperature range 350–550 °C.

Fig. 16 Schematic presentation of the pore systems in a) H-SAPO-34 (CHA topology), b) H-ZSM-5 (MFI topology), c) H-ZSM-22 (TON topology).

Fig. 17 GC-MS total ion chromatogram of hydrocarbon extracts at different time on stream. Reaction carried out over H-ZSM-22 at 400 °C, $P(CH_3OH) = 13$ kPa and $WHSV=2.05$ h^{-1} . All peaks are normalized relative to the standard peak C_2Cl_6 , indicated by * in the chromatogram. Reproduced from ¹¹⁰.

Fig. 18 Total ion gas chromatograms showing the amount and composition of the retained hydrocarbons in severely deactivated H-SAPO-34 (top) and H-ZSM-5 (bottom). The intensities are directly comparable. Reproduced from ¹⁷.

Fig. 19 a) Fluorescence intensity profiles of H-ZSM-5 crystal during the MTO reaction at 390 °C depicted with time on stream at laser excitation a) 488 nm (detection at 510–550 nm) and b) 561 nm (detection at 565–635 nm). c) Schematic representation of the slice at which the confocal fluorescence measurements were performed. The corresponding time is indicated in minutes. Reproduced from ⁹⁸.

Fig. 20 Simulated reactant conversion versus time on stream for a reaction: $A \rightarrow B$, $A \rightarrow C$, $B \rightarrow C$, where A is the reactant, B the effluent product and C the deactivating species, and where the rate constants of the three reactions are k_1 , k_2 and k_3 , respectively.

Fig. 21 Calculated conversion versus contact time curves for an autocatalytic reaction according to Eq. (2.10) and (2.11) is

represented by a solid black line. Calculated conversion for a first order reaction according to Eq. (2.10) is represented by a solid grey line. Adapted from ¹¹¹.

Fig. 22 Schematic view of the three catalyst zones in a MTH reactor. The length of each zone depends on catalyst as well as reactor conditions.

Fig. 23 C₃ (left panel) and C₅₊ aliphatic (right panel) yield as a function of conversion over various MTH catalysts at 350 °C and P(methanol)=13 kPa. Reproduced from ².

Fig. 24 James Haw's pictorial representation of a deactivating MTH catalyst (SAPO-34) as a burning cigar. Adapted from ¹⁴⁴.

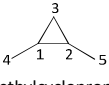
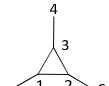
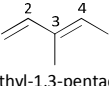
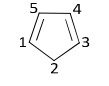
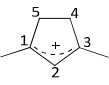
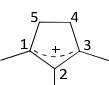
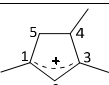
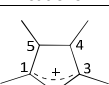
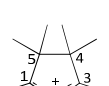
Fig. 25 Measured catalyst life times to 50% conversion as a function of contact time for H-ZSM-5 and H-ZSM-22, using P(CH₃OH) = 13 kPa. According to the autocatalytic reaction scheme, the slope of the plot equals 1/a, where a is the deactivation rate, resulting in a = 0.019 for H-ZSM-5, and a = 0.42 for H-ZSM-22. The corresponding conversion capacities are 219 g/g h for ZSM-5 and 9.9 g/g h for ZSM-22. Reproduced from ¹¹¹.

Fig. 26 Expansion of the c-axis of the unit cell of a H-SAPO-34 catalyst observed by time- and space-resolved XRD during the MTH reaction at ~340 °C, P(CH₃OH) = 13 kPa and WHSV = 3.6 g/g h. The direction of reactant flow is indicated by the large black arrows. Plot (b) is an enlargement of the first 15 minutes of plot (a). Reproduced from ¹⁵¹.

Fig. 27 Simulated concentration of reactive arene intermediates (a) and deactivating hydrocarbon deposits (b) during the reaction depicted in Figure 26. (Please note that the color coding is different from Figure 26.) The initial progress of HCP intermediates towards the bed inlet with TOS is clearly modeled, as is the formation of coke which spreads towards the outlet and causes the final expansion and deactivation. Reproduced from ¹⁵¹.

Tables

Table 1 Experimentally observed intermediates with ^{13}C NMR spectroscopy.

Intermediates	$\delta_{13\text{C}}/\text{ppm}$	Zeolites	Ref.
 dimethylcyclopropane	16.0(1,2) 14.1(3) 12.0(4,5)	H-SAPO-34	25
 trimethylcyclopropane	14.7(1,2,3) 9.8(4,5,6)	H-SAPO-34	25
 3-methyl-1,3-pentadiene	141.9(2) 135.3(3) 126.6(4) 111.8(1) 11.1(5)	H-SAPO-34	25
 cyclopentadiene	132.8(1,3) 132.2(4,5) 41.6(2)	H-SAPO-34	25
 1,3-dimethylcyclopentyl cation	250.0(1,3) 147.0(2) 48.0(4,5) 250.0(1,3) 147.0(2) 249(1,3) 146(2) 46(4,5)	H-SAPO-34 H-ZSM-5 H-ZSM-5	25 32 28
 1,2,3-trimethylcyclopentyl cation	247.0(1,3) 155.3(2) 48(4,5) 243(1,3) 155(2)	H-SAPO-34 H-ZSM-5	25 32
 1,3,4-trimethylcyclopentyl cations	247(1) 143(2) 256(3)	H-ZSM-5	32
 pentamethylcyclopentyl cation	240- 250(3,5) 154(4) 56(1,2) 247(3,5) 153(4) 58-62(1,2)	H-SSZ-13 H-Beta	31 31
 heptamethylcyclopentyl cation	253(1,3) 155(2) 56(4,5)	H-SAPO-34	34

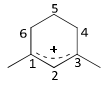
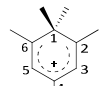
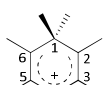
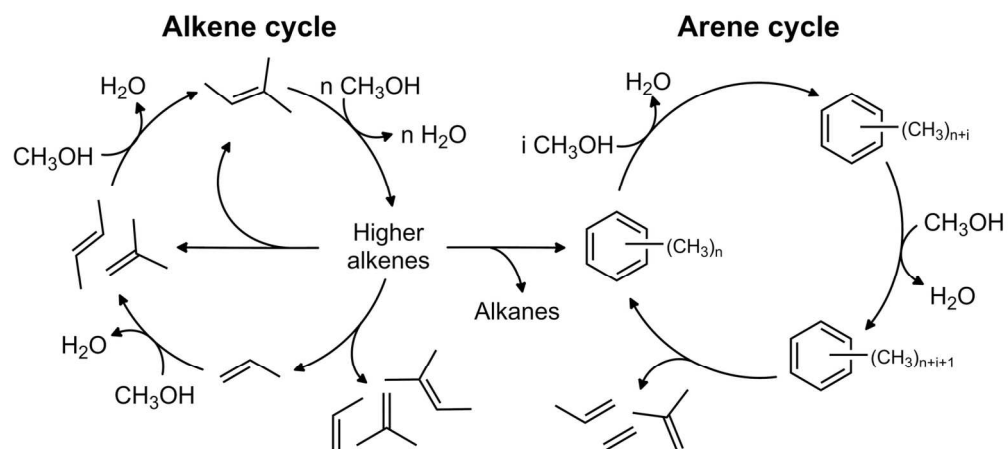
 1,3-dimethyl-2-cyclohexenyl cation	226.6(1,3) 136.8(2)	H-SAPO-34	25
 1,1,2,4,6-pentamethylbenzenium cation	206(2) 190(4) 135(3) 58(1) 205(2) 189(4) 140(3) 58(1)	H-SAPO-34 H-ZSM-5	25 32
 heptamethylbenzenium cation	198(2,6) 188(4) 152(3,5) 57(1) 198(2,6) 185(4) 141(3,5) 53(1) 203(2,6) 189(4) 144(3,5) 55(1)	H-DNL-6 H-SAPO-34 H-SSZ-13	38 31 31

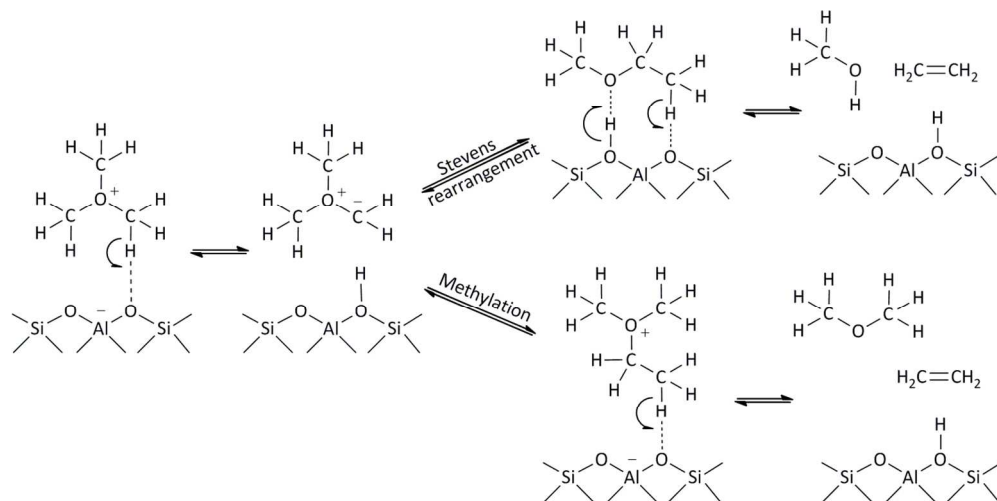
Table 2 Computational results for different direct mechanisms.

Reaction	E_r^a kJ/mol	E_a^b kJ/mol	k s^{-1}	Model	Ref.
Oxonium ylide mechanism					
ZO+TMO ⇌ ZOH+DOMY	241	--	--	5T	20
	310	--	--	46T	20
via stevens rearrangement					
ZOH+DOMY ⇌ ZOH+MEE	-352	113	1.5×10^5	5T ^c	19
	-419	133	--	46T	20
via intermolecular methylation					
ZOCH ₃ +DOMY ⇌ ZO+EDMO	-306	17.9	6.6×10^{10}	5T ^c	19
	-381	≈ 0	--	46T	20
Carbene mechanism					
ZOCH ₃ ⇌ ZOH+:CH ₂	166	221	--	3T	68
	191	242	5.3×10^{-7}	5T ^c	19
Methane-formaldehyde mechanism					
ZOCH ₃ +CH ₃ OH+H ₂ O ⇌ ZOH+CH ₂ O+CH ₄ +H ₂ O	-50	147	4.0×10^0	5T ^c	19
ZOCH ₃ +CH ₃ OH ⇌ ZOH+ CH ₂ O+CH ₄	--	171	--	1T	75
	-50	148	--	3T	76
	-44	189	7.2×10^{-3}	5T ^c	19
	--	150	2.1×10^3	Periodic ^d	53
ZOH+CH ₂ O+CH ₄ ⇌ ZOH+ CH ₃ CH ₂ OH	-72	185	--	3T	76
	-46	183	1.7×10^{-6}	5T ^c	19
	--	125	7.4×10^{-1}	Periodic ^d	53
Methoxymethyl cation mechanism					
ZOCH ₃ +CH ₃ OCH ₃ ⇌ ZO ⁺ +CH ₃ OCH ₂ ⁺ +CH ₄	55	135	1.1×10^4	Periodic ^d	53
ZO ⁺ +CH ₃ OCH ₂ ⁺ +CH ₃ OCH ₃ ⇌ ZOH+CH ₃ OCH ₂ CH ₂ OCH ₃	-176	95	6.8×10^4	Periodic ^d	53

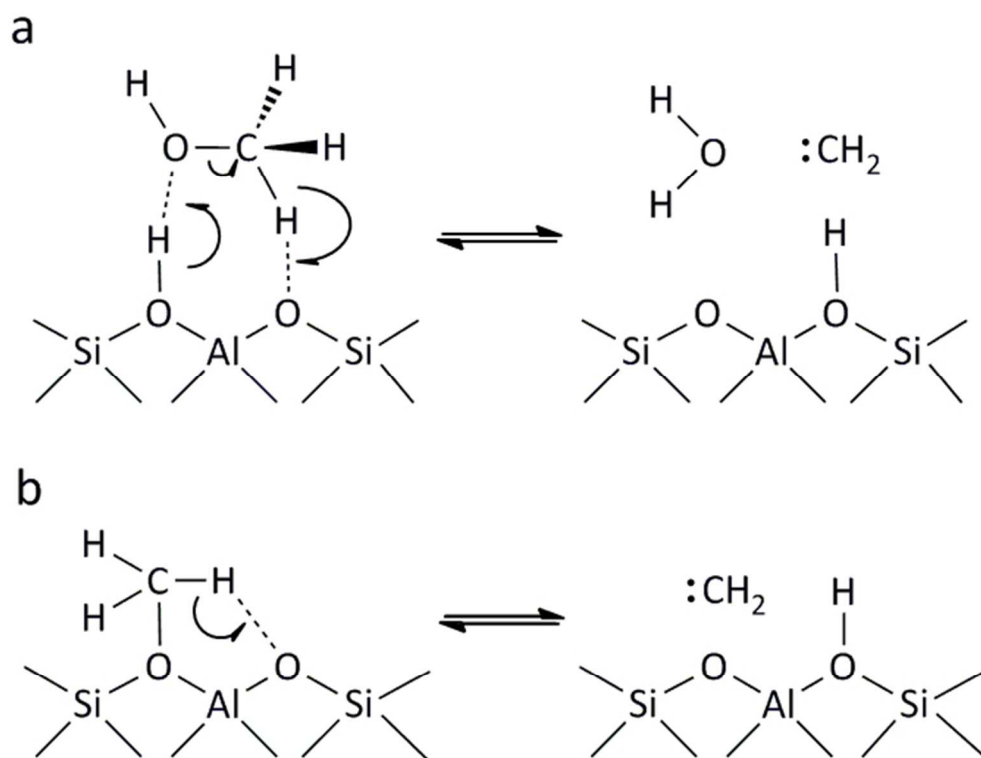
^aHeat of reaction. ^bEnergy barrier. ^cCalculated rate constant at 447 °C. ^dCalculated rate constant at 350 °C



The "dual-cycle" mechanism. Reproduced from 18.
65x29mm (600 x 600 DPI)

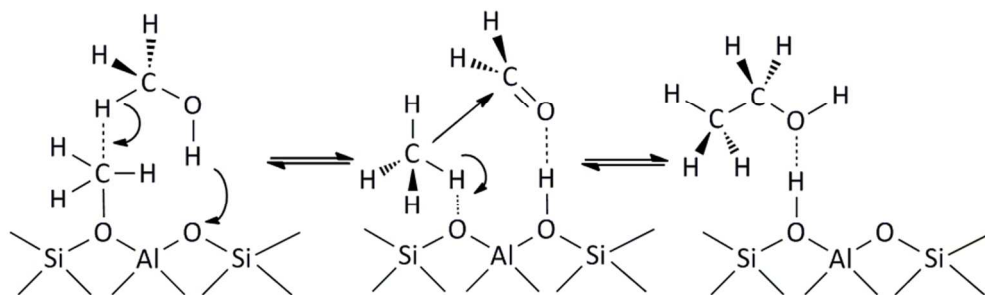


Schematic illustration of oxonium ylide mechanism.
123x62mm (300 x 300 DPI)

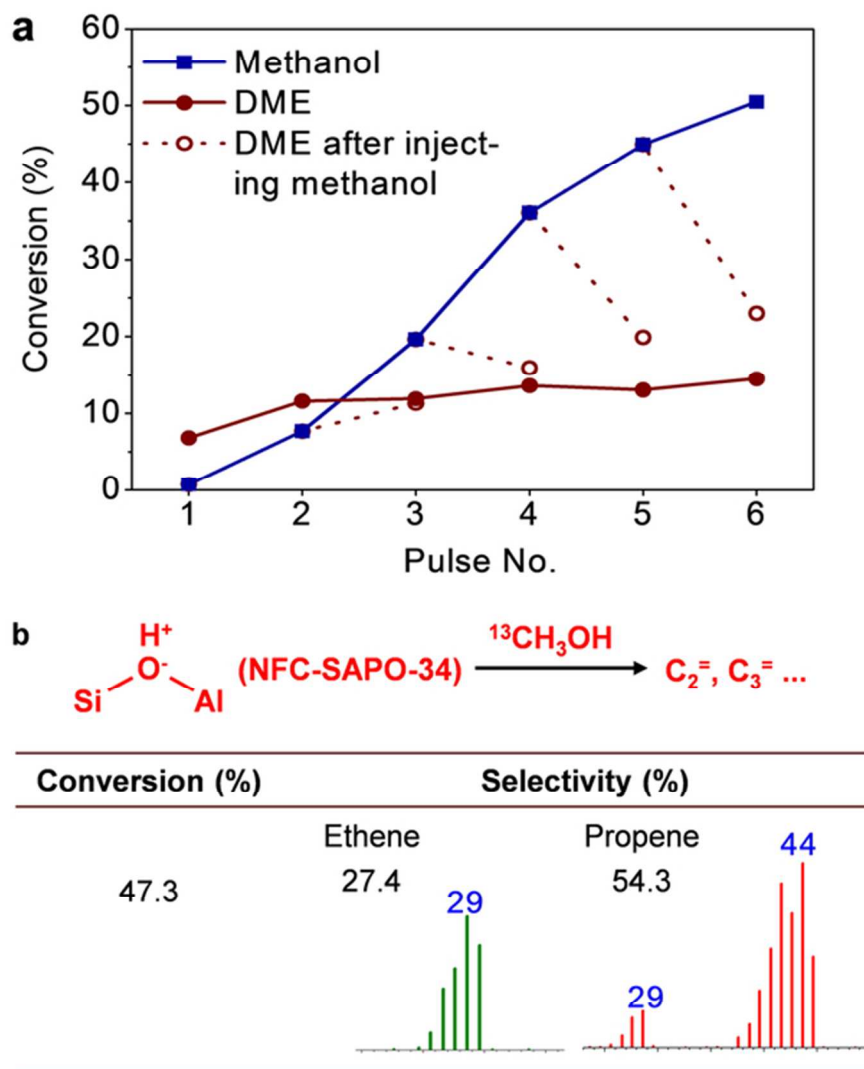


Schematic routes of carbene mechanism (a) α -elimination of water from methanol; (b) decomposition of SMS.

57x46mm (300 x 300 DPI)

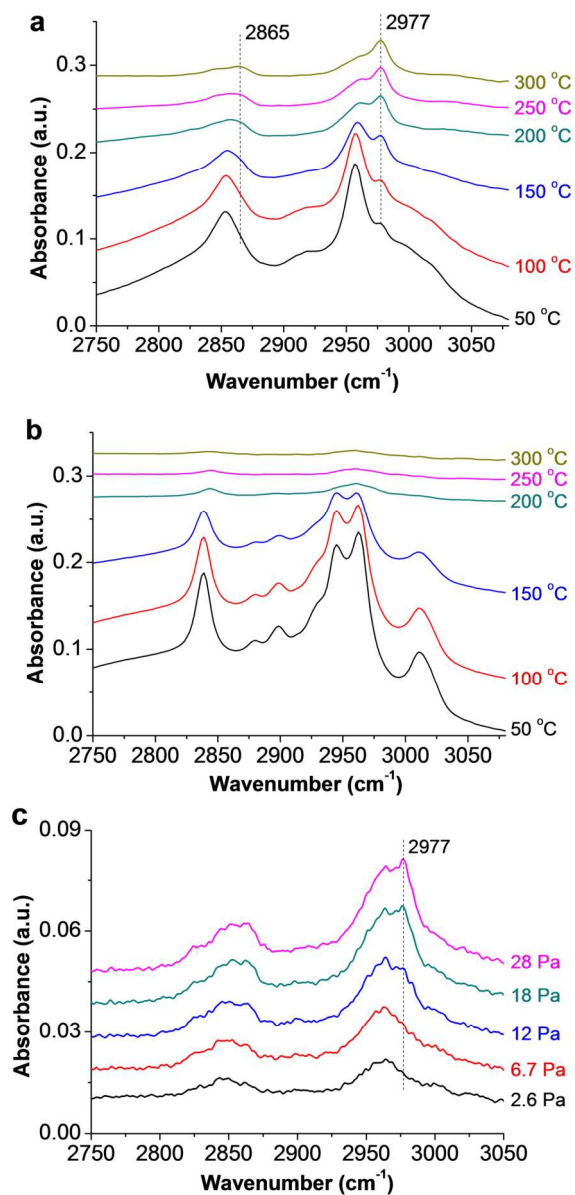


Schematic illustration of methane-formaldehyde mechanism.
83x25mm (300 x 300 DPI)

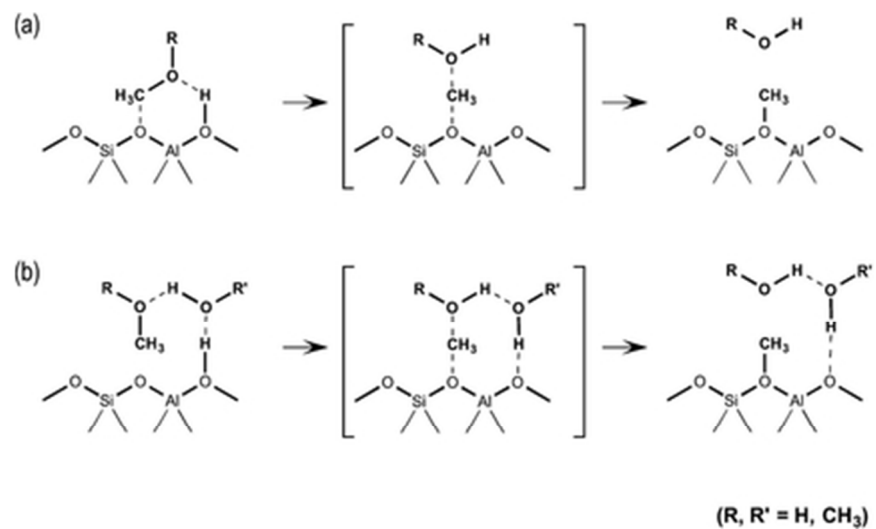


Experimental evidence for the direct mechanism. (a) Methanol (blue square) and DME (brown solid circle) conversions obtained at different pulses in the MTO process catalyzed by FC-SAPO-34 and the DME conversions (brown hollow circle) attained after successively injecting various times of methanol, e.g. the DME conversions at the pulse of 3, 4, 5 and 6 refer to the values obtained by pulsing DME after successive injection of 2, 3, 4 and 5 times of methanol. Experimental methods: 100 mg of FC-SAPO-34 was first pretreated at 550 oC for 2 h in air before the reaction, which was carried out at 400 oC with Ar as carrier gas, the flow rate of which is 300 mL/min. Every time 0.07 mmol of methanol or 0.035 mmol of DME was injected. The methanol and DME conversions were calculated by considering both of them in the effluents as unreacted substrates. (b) Reaction results of ^{13}C -methanol over the NFC-SAPO-34, which was activated at 550 oC in Ar atmosphere before pulsing 0.005 mmol of ^{13}C -methanol. Reproduced from 53.

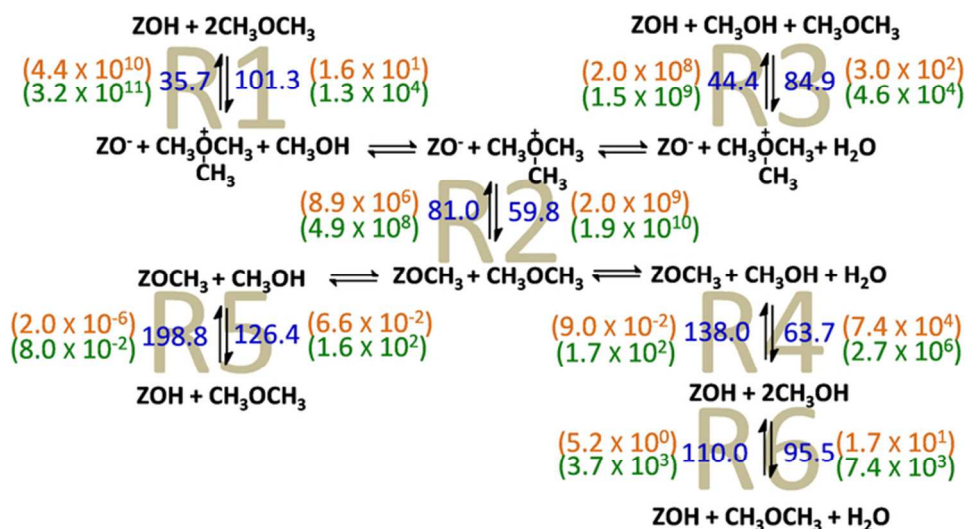
58x67mm (300 x 300 DPI)



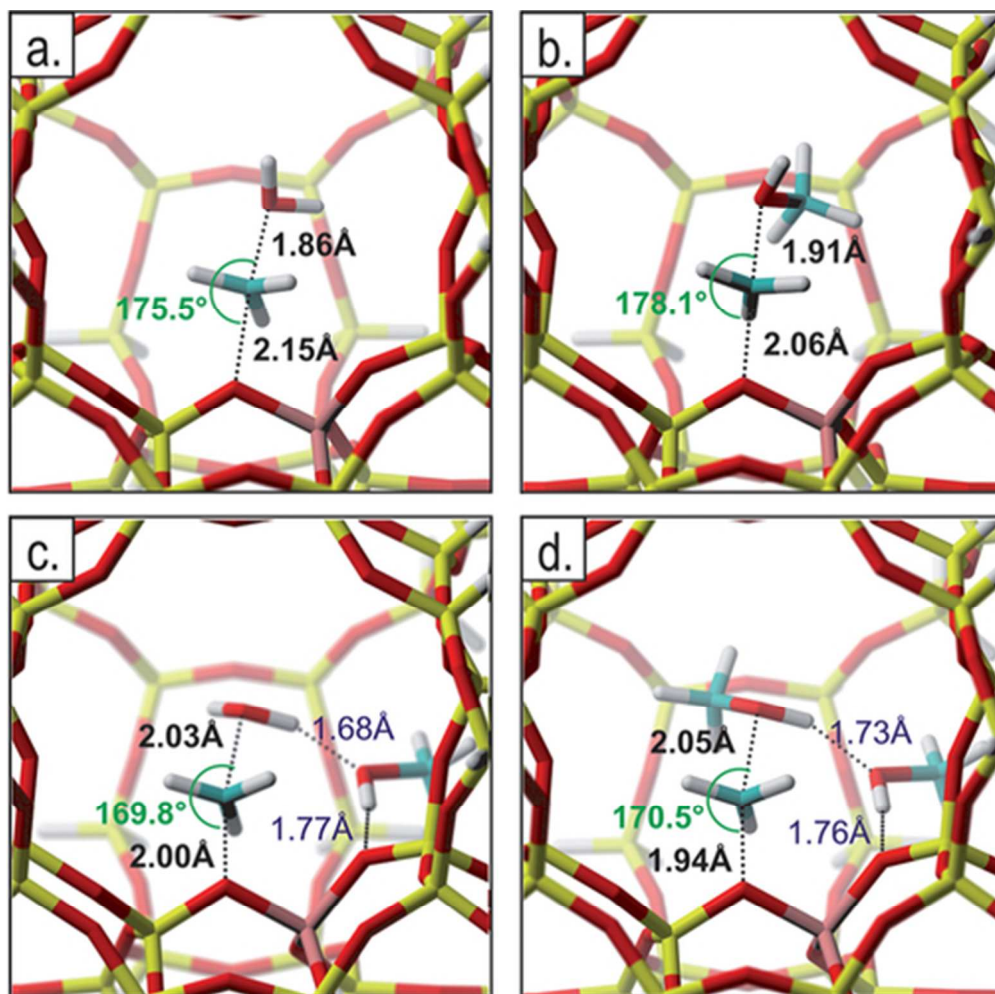
IR spectra for the formation of methoxy groups from methanol and DME. (a) 200 Pa of methanol was introduced into the IR cell equipped with 30 mg of FC-SAPO-34 self-supported wafer at 50 $^{\circ}\text{C}$. The spectra were recorded from 50 to 300 $^{\circ}\text{C}$ with the temperature ramp rate of 5 $^{\circ}\text{C}/\text{min}$. (b) 200 Pa of DME was introduced as reactant and spectra were obtained according to the same procedures as those employed in Fig. 6(a). (c) DME reacted at 300 $^{\circ}\text{C}$ for 30 s at different pressures.
106x221mm (300 x 300 DPI)



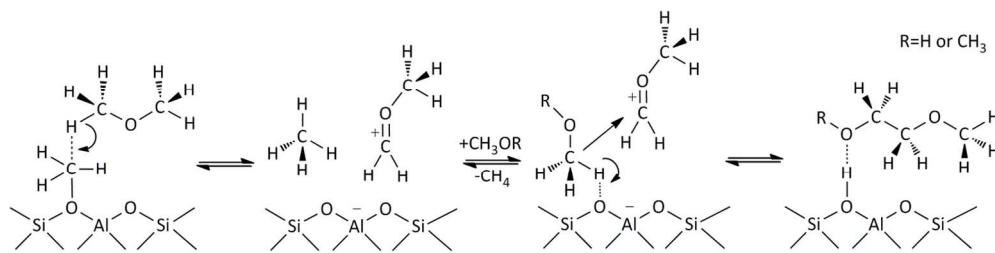
(a) Unassisted and (b) assisted methoxide formation. Reproduced from 88. 36x21mm (300 x 300 DPI)



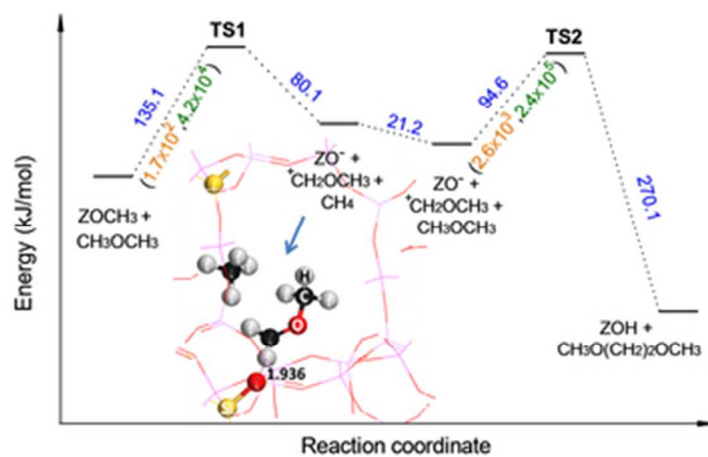
DFT calculation results for the formation of methoxy group from methanol or DME (The blue numbers represent the energy barriers (kJ/mol), while the orange and green numbers in parentheses are their rate constants (s⁻¹) at 250 and 400 °C respectively). Reproduced from 53.
67x37mm (300 x 300 DPI)



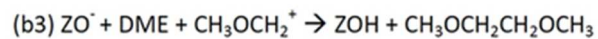
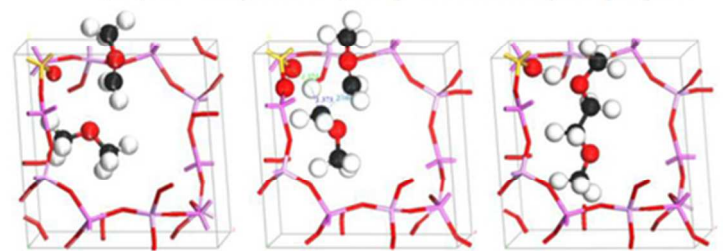
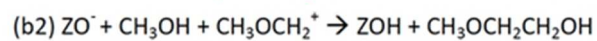
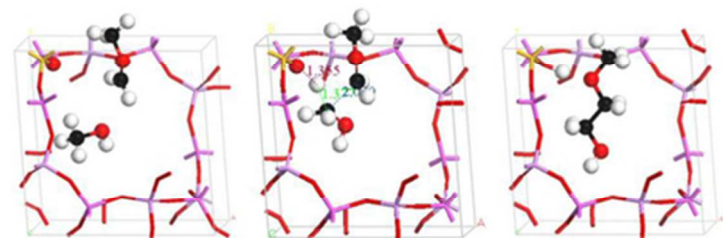
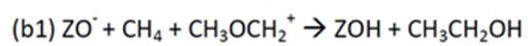
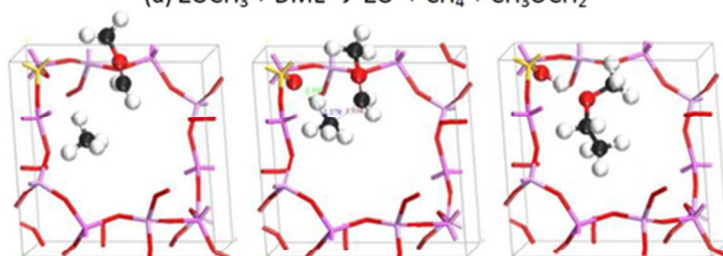
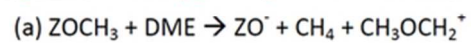
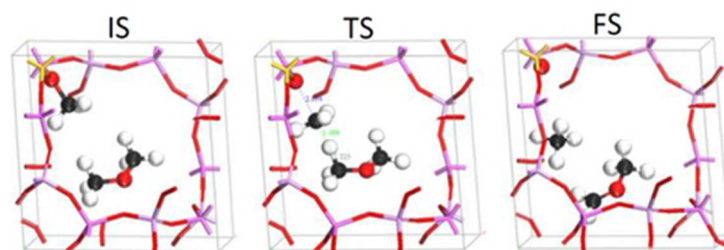
Transition states for a,b) unassisted and c,d) methanol-assisted methoxide formation from a,c) methanol and b,d) dimethyl ether. Reproduced from 88.
42x42mm (300 x 300 DPI)



Schematic illustration of the methoxymethyl mechanism.
126x31mm (300 x 300 DPI)

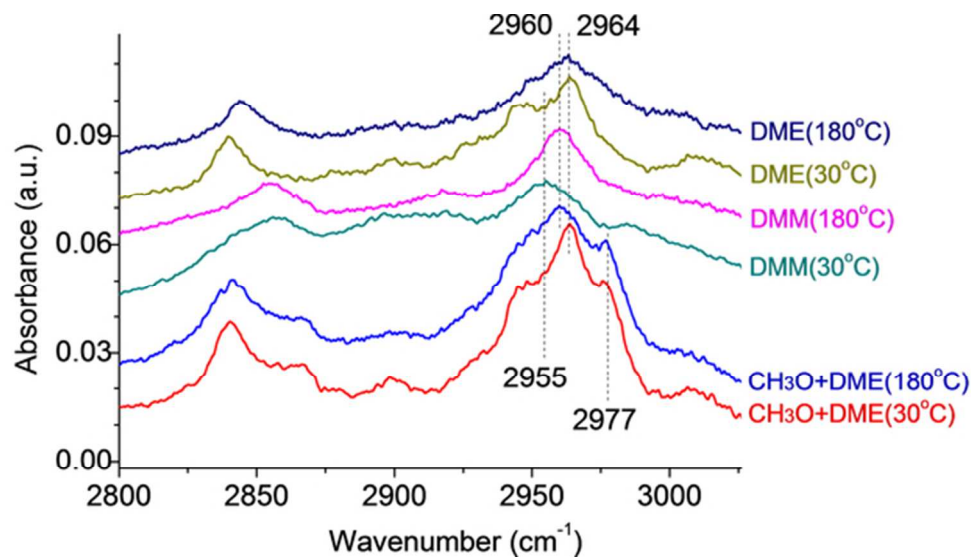


Route for the formation of the first C-C bond from surface methoxy and DME. The blue numbers represent the energy barriers (kJ/mol), while the orange and green numbers in parentheses are the rate constants (s⁻¹) at 250 and 400 °C respectively. Reproduced from 53.
32x20mm (300 x 300 DPI)



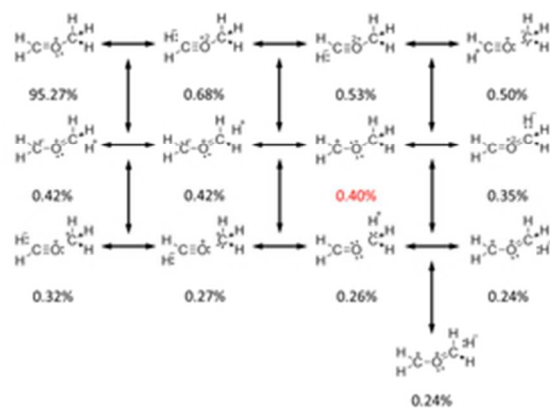
The structures of initial states, transition states and final states of the two steps in the methoxymethyl mechanism.

40x65mm (300 x 300 DPI)

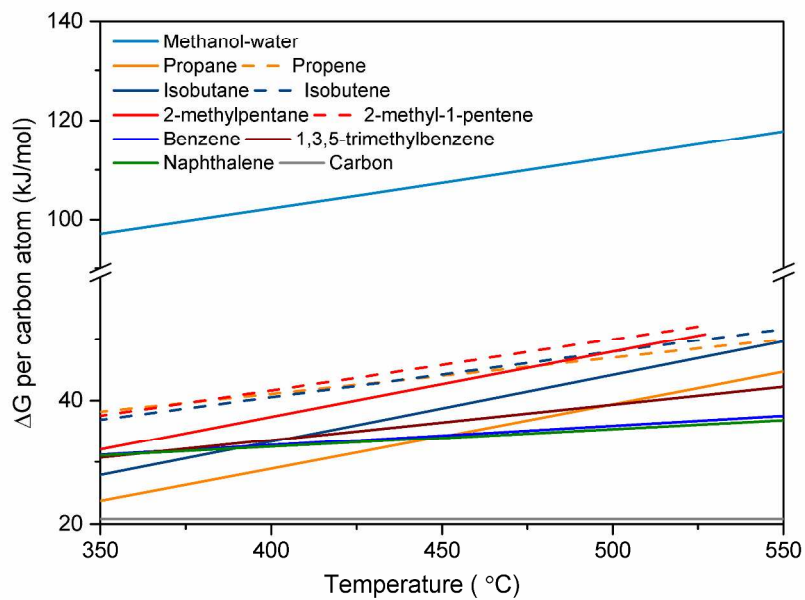


IR spectra for the formation of $\text{CH}_3\text{OCH}_2^+$ by the reaction of methoxy group and DME. Experimental methods: 6.5 Pa of DME was introduced into the IR cell equipped with 30 mg of CH_3O -formed FC-SAPO-34 self-supported wafer at 30 oC. The spectra were recorded from 30 to 180 oC with a temperature ramp rate of 5 oC/min. The spectra recorded at 30 and 180 oC were denoted as $\text{CH}_3\text{O}+\text{DME}(30\text{oC})$ and $\text{CH}_3\text{O}+\text{DME}(180\text{oC})$ respectively. The spectra of $\text{DMM}(30\text{oC})$ and $\text{DMM}(180\text{oC})$ were obtained by introducing 6.5 Pa of dimethoxymethane into the IR cell equipped with 30 mg of the pretreated FC-SAPO-34 self-supported wafer at 30oC, and then increasing the temperature to 180 oC. The spectra of $\text{DME}(30\text{oC})$ and $\text{DME}(180\text{oC})$ were obtained according to the same procedures as those employed for measuring $\text{DMM}(30\text{oC})$ and $\text{DMM}(180\text{oC})$ except that DME was introduced. Reproduced from 53.

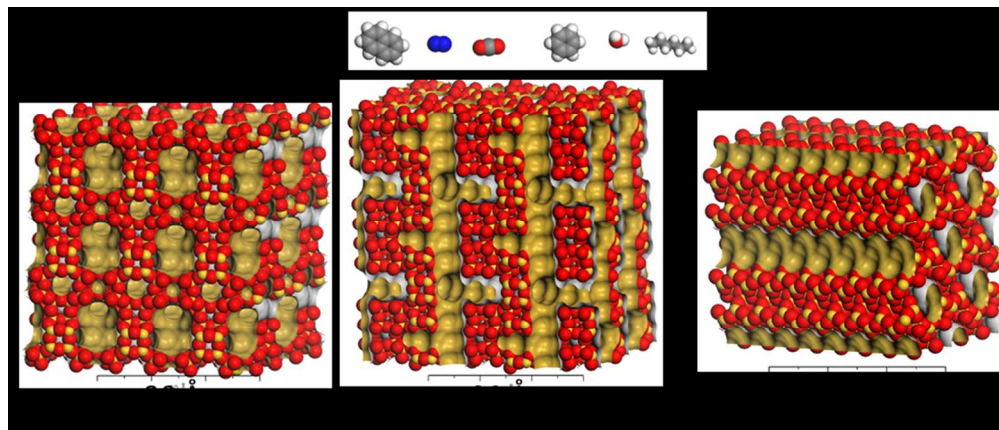
54x29mm (300 x 300 DPI)



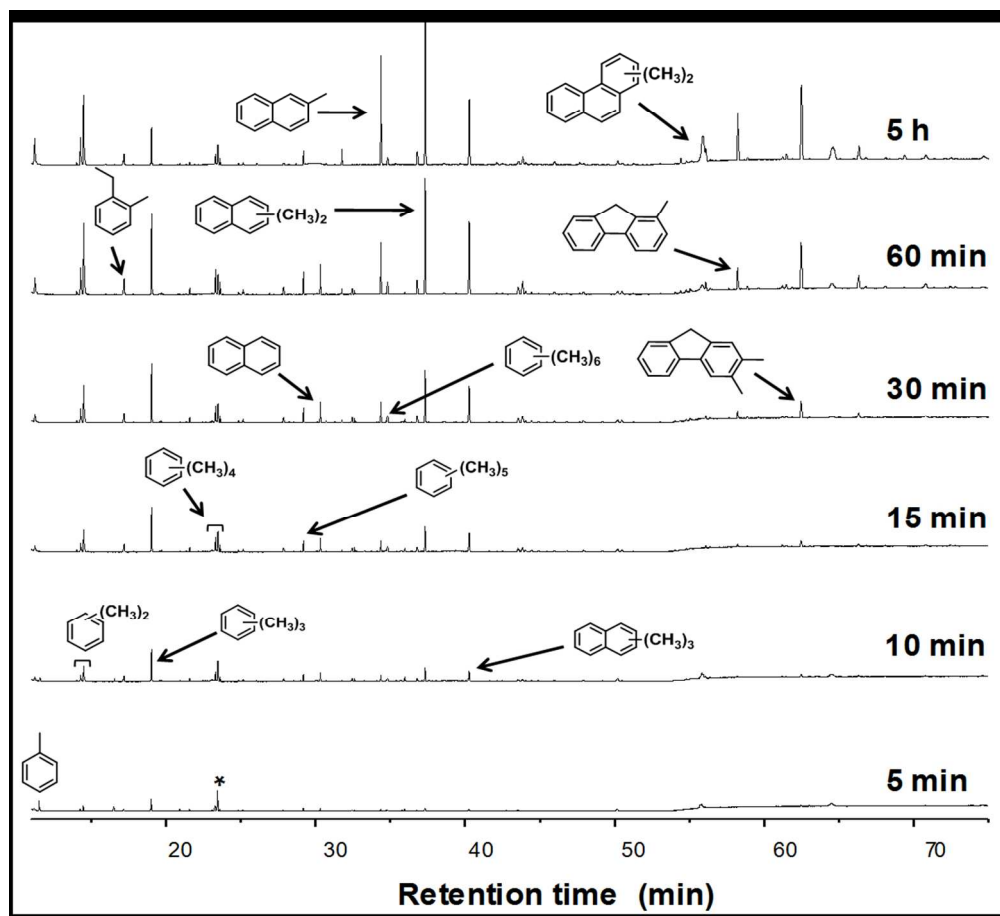
NRT analysis of $(\text{CH}_2\text{OCH}_3)^+$ ion at MP2/cc-pVQZ level.
23x16mm (300 x 300 DPI)



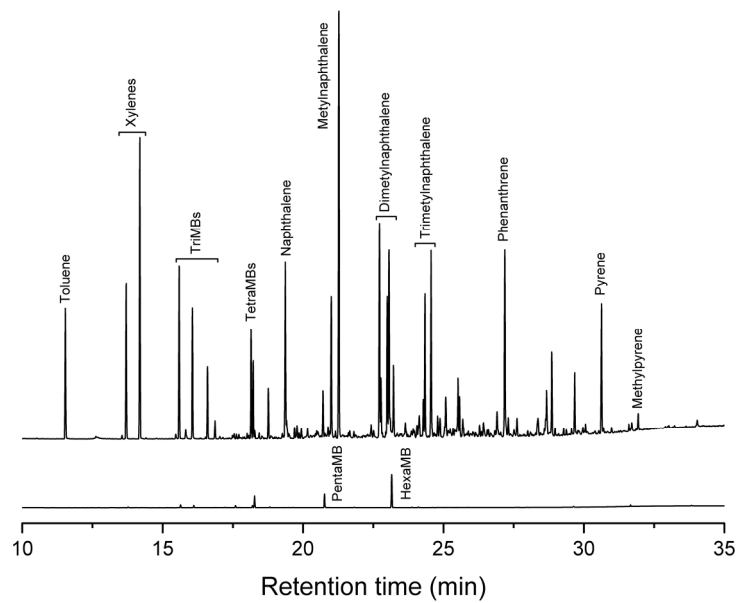
Gibbs energy of formation per C atom (kJ/mol) for reactant and product molecules associated with the MTH process in the temperature range 350-550 °C.
287x201mm (300 x 300 DPI)



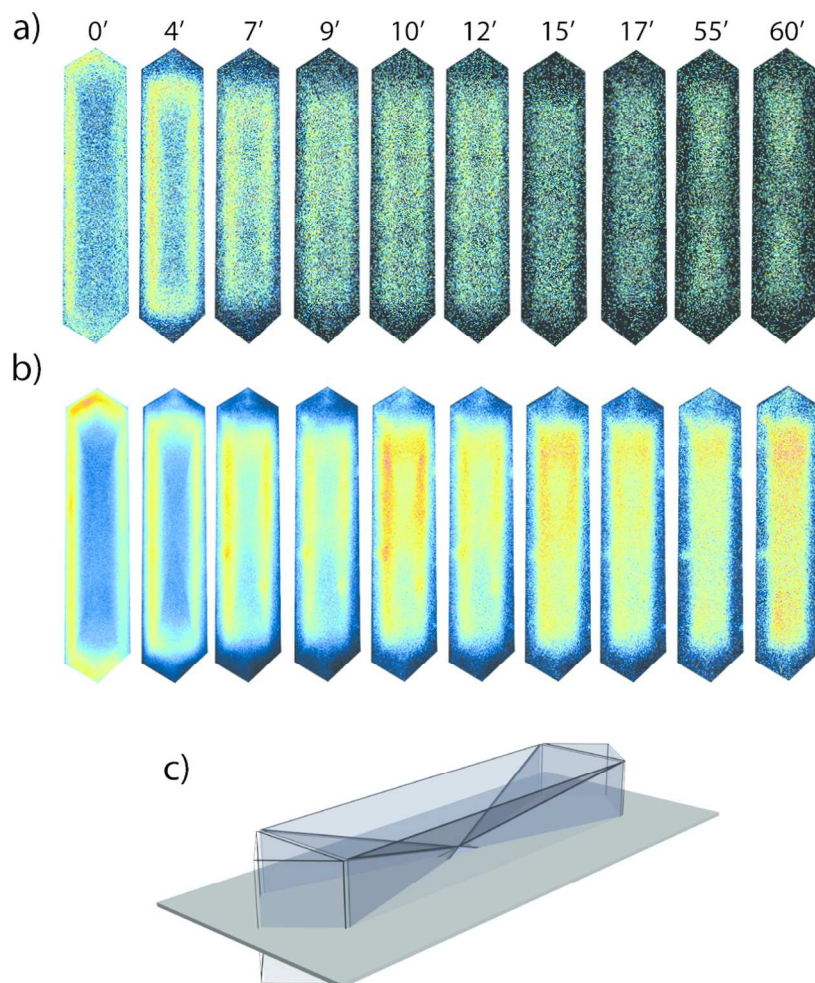
Schematic presentation of the pore systems in a) H-SAPO-34 (CHA topology), b) H-ZSM-5 (MFI topology), c) H-ZSM-22 (TON topology).
88x37mm (300 x 300 DPI)



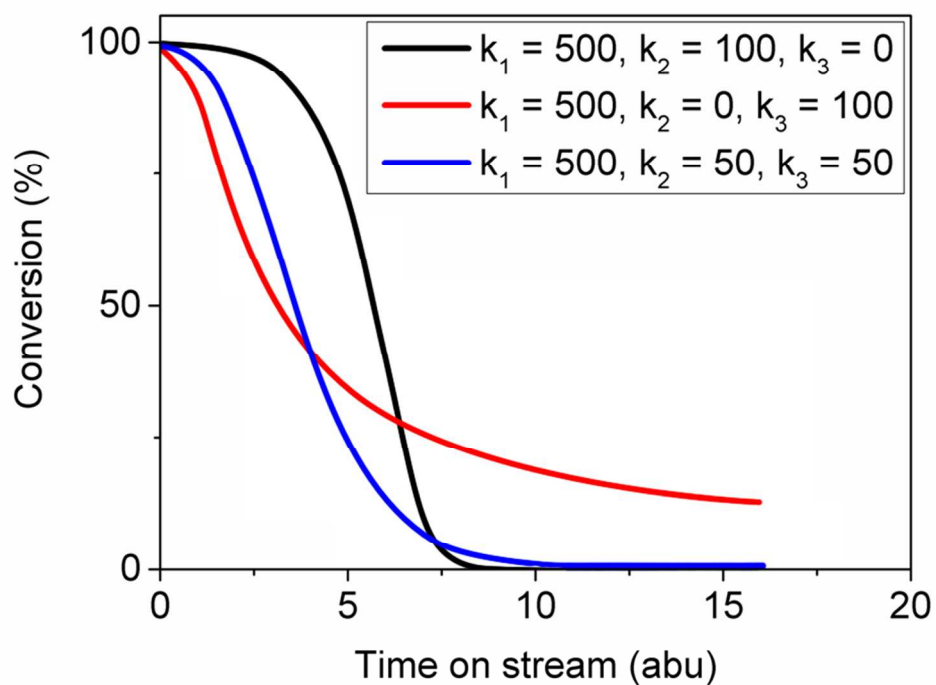
GC-MS total ion chromatogram of hydrocarbon extracts at different time on stream. Reaction carried out over H-ZSM-22 at 400 °C, P(CH₃OH) = 13 kPa and WHSV=2.05 h⁻¹. All peaks are normalized relative to the standard peak C₂Cl₆, indicated by * in the chromatogram. Reproduced from 110. 204x186mm (150 x 150 DPI)



Total ion gas chromatograms showing the amount and composition of the retained hydrocarbons in severely deactivated H-SAPO-34 (top) and H-ZSM-5 (bottom). The intensities are directly comparable. Reproduced from 17.
201x140mm (300 x 300 DPI)

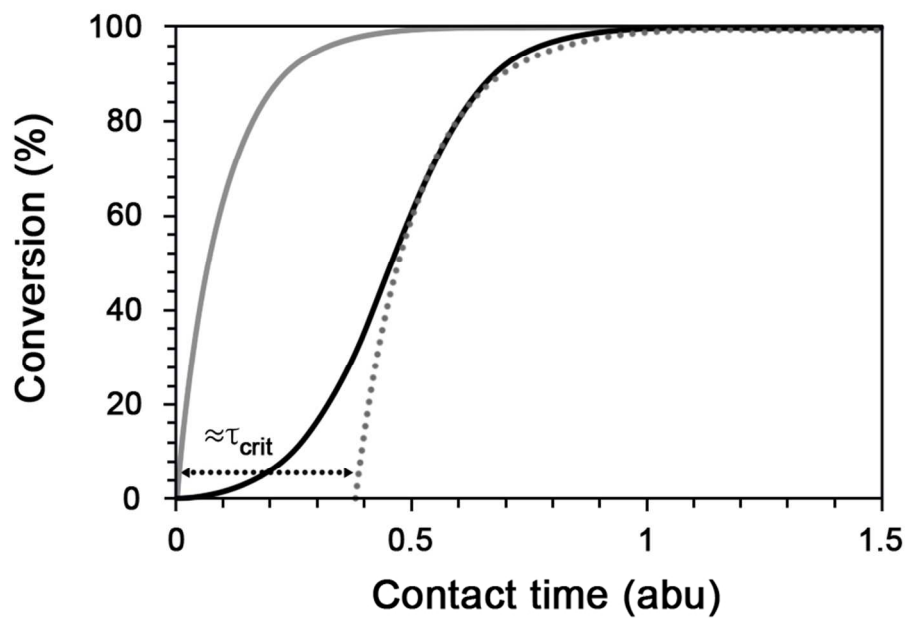


a) Fluorescence intensity profiles of H-ZSM-5 crystal during the MTO reaction at 390 °C depicted with time on stream at laser excitation a) 488 nm (detection at 510–550 nm) and b) 561 nm (detection at 565–635 nm). c) Schematic representation of the slice at which the confocal fluorescence measurements were performed. The corresponding time is indicated in minutes. Reproduced from 98.
105x132mm (300 x 300 DPI)

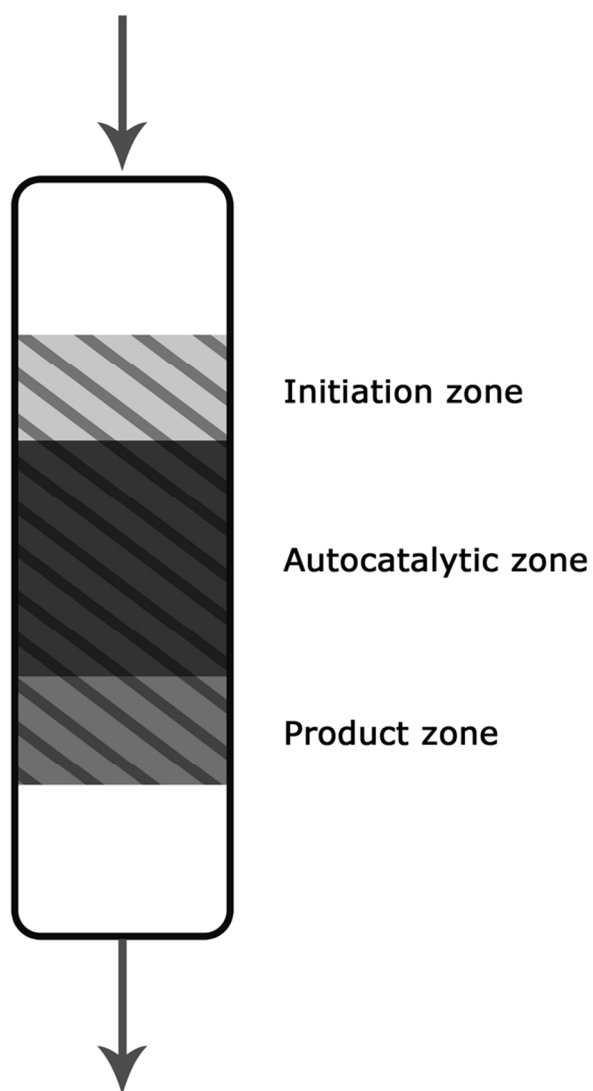


Simulated reactant conversion versus time on stream for a reaction: $A \rightarrow B$, $A \rightarrow C$, $B \rightarrow C$, where A is the reactant, B the effluent product and C the deactivating species, and where the rate constants of the three reactions are k_1 , k_2 and k_3 , respectively.

83x63mm (300 x 300 DPI)

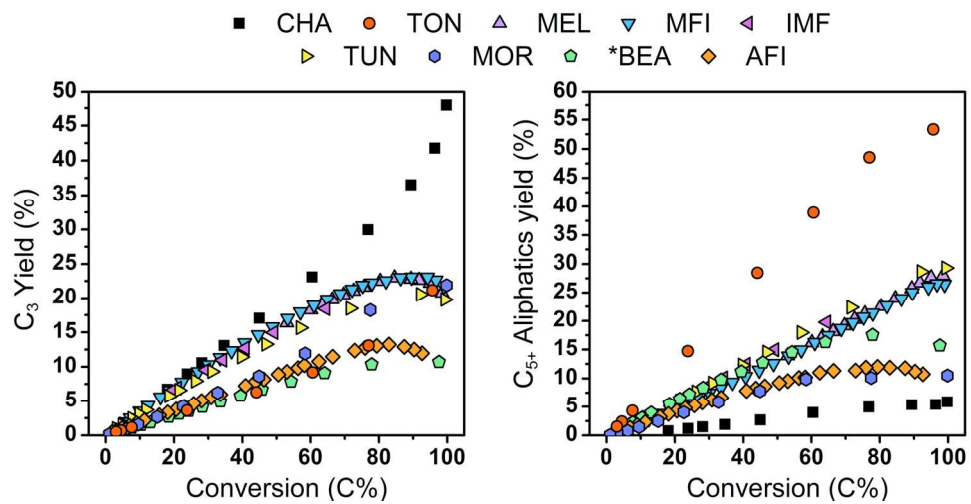


Calculated conversion versus contact time curves for an autocatalytic reaction according to Eq. (2.10) and (2.11) is represented by a solid black line. Calculated conversion for a first order reaction according to Eq. (2.10) is represented by a solid grey line. Adapted from 111.
88x64mm (300 x 300 DPI)

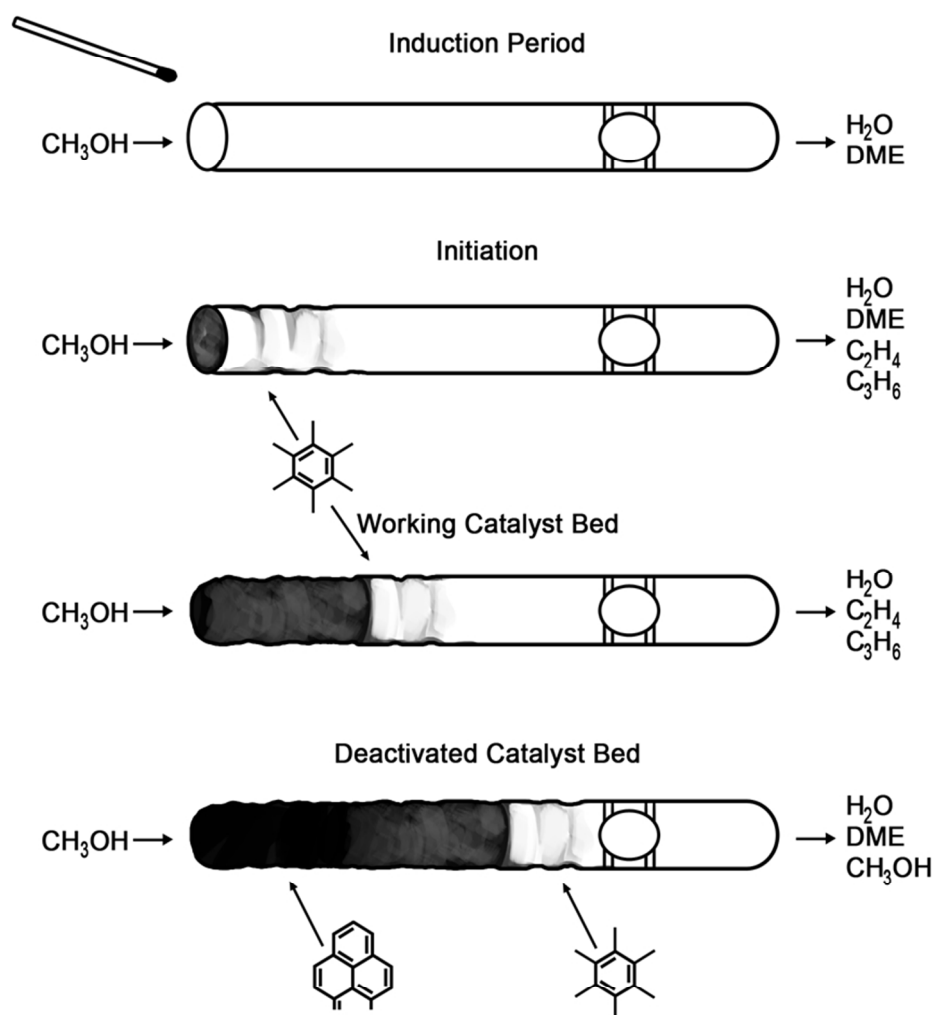


Schematic view of the three catalyst zones in a MTH reactor. The length of each zone depends on catalyst as well as reactor conditions.

75x115mm (299 x 299 DPI)

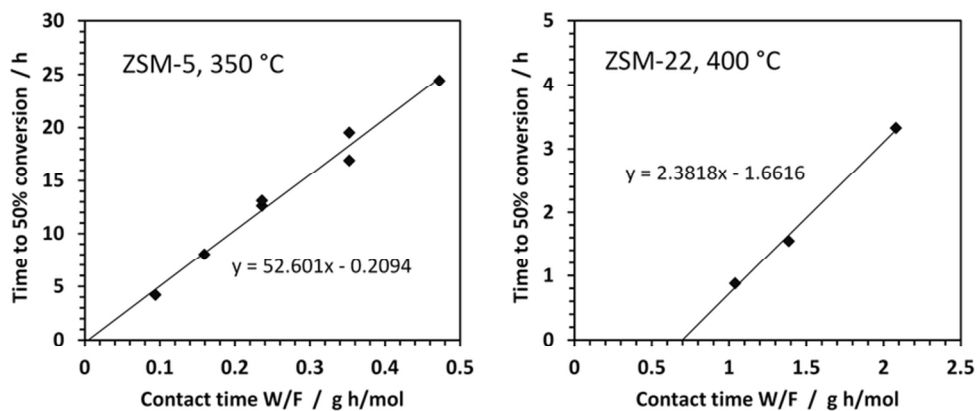


C₃ (left panel) and C₅₊ aliphatic (right panel) yield as a function of conversion over various MTH catalysts at 350 °C and P(methanol)=13 kPa. Reproduced from 2.
80x40mm (600 x 600 DPI)



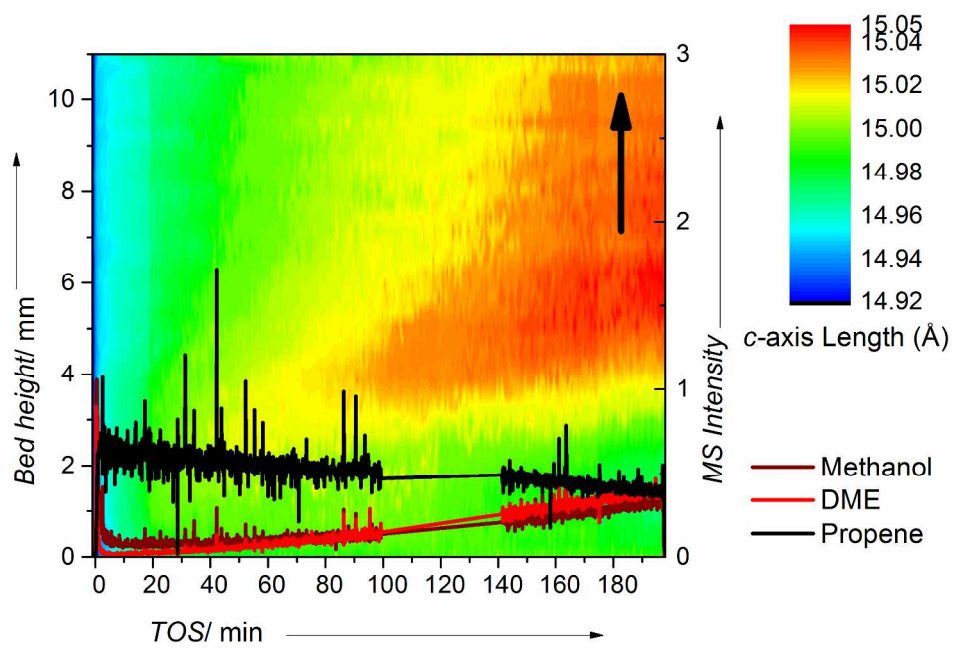
James Haw's pictorial representation of a deactivating MTH catalyst (SAPO-34) as a burning cigar. Adapted from 144.

327x371mm (72 x 72 DPI)

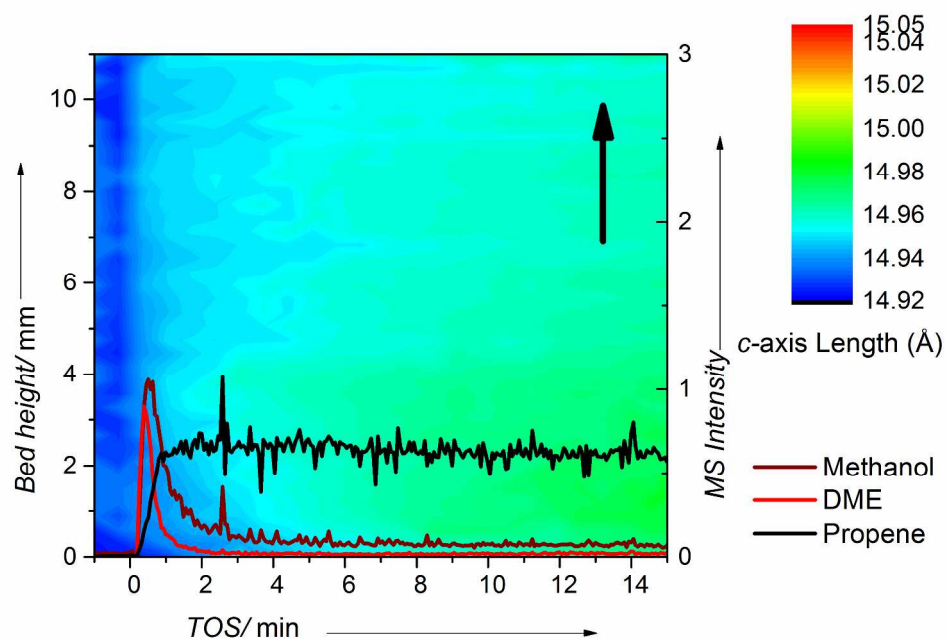


Measured catalyst life times to 50% conversion as a function of contact time for H-ZSM-5 and H-ZSM-22, using $P(\text{CH}_3\text{OH}) = 13 \text{ kPa}$. According to the autocatalytic reaction scheme, the slope of the plot equals $1/a$, where a is the deactivation rate, resulting in $a = 0.019$ for H-ZSM-5, and $a = 0.42$ for H-ZSM-22. The corresponding conversion capacities are 219 g/g h for ZSM-5 and 9.9 g/g h for ZSM-22. Reproduced from 111.

74x32mm (300 x 300 DPI)

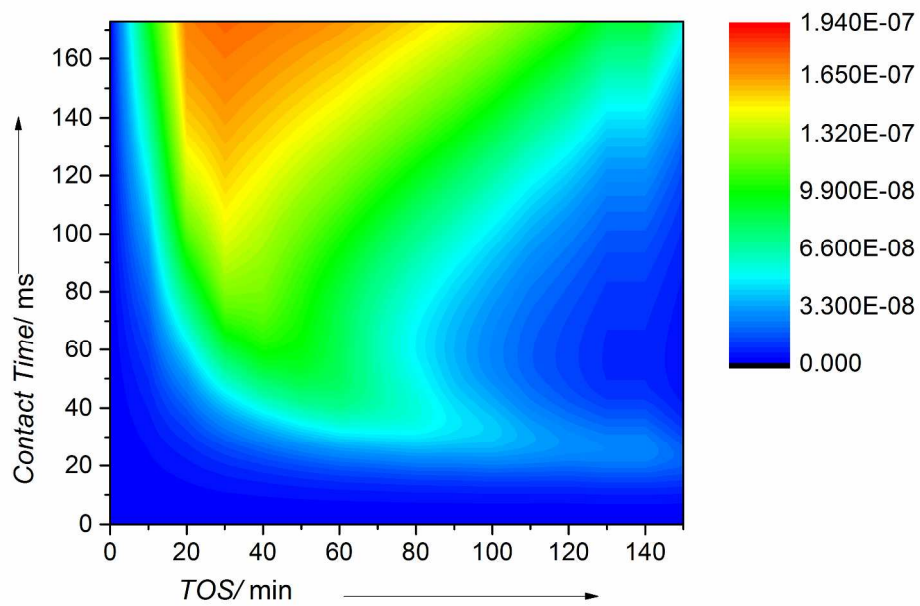


287x201mm (300 x 300 DPI)

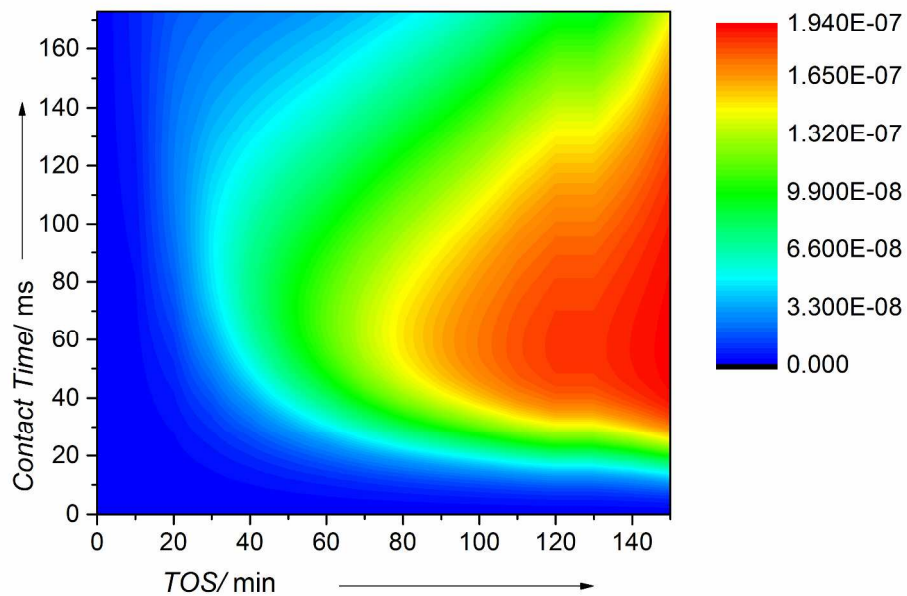


Expansion of the c-axis of the unit cell of a H-SAPO-34 catalyst observed by time- and space-resolved XRD during the MTH reaction at ~ 340 °C, $P(\text{CH}_3\text{OH}) = 13$ kPa and $\text{WHSV} = 3.6$ g/g h. The direction of reactant flow is indicated by the large black arrows. Plot (b) is an enlargement of the first 15 minutes of plot (a).

Reproduced from 151.
287x201mm (300 x 300 DPI)



287x201mm (300 x 300 DPI)



Simulated concentration of reactive arene intermediates (a) and deactivating hydrocarbon deposits (b) during the reaction depicted in Figure 26. (Please note that the color coding is different from Figure 26.) The initial progress of HCP intermediates towards the bed inlet with TOS is clearly modeled, as is the formation of coke which spreads towards the outlet and causes the final expansion and deactivation. Reproduced from 151.

287x201mm (300 x 300 DPI)